

Projection-based model reduction of dynamical systems using space-time subspace and machine learning

Chi Hoang* Kenny Chowdhary* Kookjin Lee* Jaideep Ray*

Abstract

This paper considers the creation of parametric surrogate models for applications in science and engineering where the goal is to predict high-dimensional spatiotemporal output quantities of interest, such as pressure, temperature and displacement fields. The proposed methodology develops a low-dimensional parametrization of these quantities of interest using space-time bases combining with machine learning methods. In particular, the space-time solutions are sought in a low-dimensional space-time *linear* trial subspace that can be obtained by computing tensor decompositions of usual state-snapshots data. The mapping between the input parameters and the basis expansion coefficients (or generalized coordinates) is approximated using four different machine learning techniques: multivariate polynomial regression, k-nearest-neighbors, random forest and neural network. The relative costs and effectiveness of the four machine learning techniques are explored through three engineering problems: steady heat conduction, unsteady heat conduction and unsteady advective-diffusive-reactive system. Numerical results demonstrate that the proposed method performs well in terms of both accuracy and computational cost, and highlight the important point that the amount of model training data available in an engineering setting is often much less than it is in other machine learning applications, making it essential to incorporate knowledge from physical models. In addition, simpler machine learning techniques are seen to perform better than more elaborate ones.

Keywords: model reduction, data-driven reduced models, physics-based machine learning, space-time bases, surrogate models, non-intrusive reduced models

1 Introduction

Many tasks in computational science and engineering are *many query* in nature, as they require the repeated simulations of a parameterized large-scale computational model. Model reduction has become a popular approach to make such tasks tractable. Most of such techniques first perform an “offline” training stage that simulates the computational model for multiple input-parameter instances to build a low-dimensional subspace or manifold. Then during an “online” deployed stage, these techniques reduce the dimensionality and complexity of the original computational model at arbitrary unseen input-parameter instances by performing a projection process of the original computational model onto that low-dimensional subspace or manifold. The projection framework can be combined with various ways of representing parametric dependence, where the input parameters might describe, for example, material properties, system geometry, system configuration, initial conditions and/or boundary conditions. The output generally consists of quantities of interest in the form of whole fields or some extractions/functions of the field such as pressure, temperature or displacement fields.

For initial boundary value problems, many model reduction approaches based on time and frequency domains have been proposed. In particular, moment-matching methods are commonly used for frequency domain-based model reduction, such as the Lanczos algorithm [1], the Arnoldi algorithm [2], and the Krylov

*Extreme-scale Data Science and Analytics Department, Sandia National Laboratories, Livermore, CA 94550 (ckhoang@sandia.gov). Sandia National Laboratories is a multimission laboratory managed and operated by National Technology and Engineering Solutions of Sandia, LLC, a wholly owned subsidiary of Honeywell International, Inc., for the U.S. Department of Energy’s National Nuclear Security Administration under contract DE-NA-0003525.

subspace method [3, 4]. These moment-matching techniques are primarily applicable to model reduction of linear time-invariant systems. Time domain-based model reduction techniques can be divided into several types, such as the balanced truncation method [5], the proper orthogonal decomposition (POD) method [6], the reduced basis (RB) method [7], the proper generalized decomposition (PGD) method [8], and recently the dynamic modes decomposition (DMD) method [9], to name just a few. We are also aware of several hyper-reduction techniques that can be used to enhance some of the aforementioned methods such as the Missing Point Estimation method [10], the Gauss–Newton with approximated tensors (GNAT) [11], the Empirical Interpolation Method (EIM) [12], and its discrete variant the Discrete Empirical Interpolation Method (DEIM) [13], etc.

Alternatively, another approach involves learning the mapping from input parameters to output low-dimensional representations of the high-fidelity model data (i.e., generalized coordinates or basis expansion coefficients). That is, these methods first (i) build off a set of “snapshots” that are solutions associated with the high-fidelity model for different input-parameter instances; then (ii) project snapshot data onto a low-dimensional subspace and finally (iii) use the low-dimensional, projected snapshots as training data to build the reduced models as mappings from the inputs to the output basis expansion coefficients (or output generalized coordinates). Both classical interpolation and standard machine-learning-based methods have been used to determine such mappings. Perhaps the earliest example that approximates such an input-output mapping can be found in [14], in which the authors compute a POD representation of the temperature field in a Rayleigh–Bénard convection problem, and then uses a cubic spline interpolation to predict the temperature field at Rayleigh numbers that are not included in the snapshot training data. Ref. [15] reconstructs POD representations of aerodynamic quantities from incomplete data using interpolation via gappy POD [16]. Other approaches use Gaussian process regression to build a model for the POD coefficients as a function of the inputs [17, 18, 19]. The authors in Ref. [20] learn the mapping from inputs to POD coefficients using an adaptive combination of self-organizing maps and local response surfaces, while [21, 22] learns the mapping from inputs to POD coefficients using neural networks. In Ref. [23], learning the POD coefficients is coupled with a greedy approach to actively guide the sampling in the input domain. Interestingly, the work in Ref. [24] approximates the mapping between input parameters and the POD coefficients by exploring various machine learning (ML) methods, and partly inspires this current paper.

Instead of learning a mapping from the inputs to the coefficients of POD representations, data-driven model reduction seeks to learn the *operators* of reduced models (or more of system identification or operator regression). Thus, these data-driven model reduction techniques provide a way to learn the *dynamics* of the system of interest in the form of reduced-model operators that respect some of the structure of the underlying governing equations. Data-driven model reduction shares similarities with classical system identification [25], where dynamical system models are extracted from time- and frequency-domain measurements. The eigensystem realization algorithm [26, 27] and finite impulse response system identification [28] are two system identification techniques that seek to learn reduced models from impulse responses of linear time-invariant systems. Vector fitting is a regression-based approach to learn a reduced model from frequency-response data [29]. Data-driven model reduction methods based on dynamic mode decomposition learn linear reduced operators that best-fit given data in the ℓ_2 norm [30]. The work in [31] uses least-squares regression to find operators in a similar way to dynamic mode decomposition but is applicable to models with low-order polynomial terms. The work in [32] uses a recursive variable selection strategy to learn a reduced model, with a focus on retaining physical interpretability. A different line of work leverages (data) sparsity-promoting regression techniques to learn reduced models from data such as in [33, 34, 35, 36].

Despite this wealth of literature, it seems that no work has sought to construct a map between input parameters and space-time bases expansion coefficients. In comparison with spatial bases reduced order modeling, the main benefit of space-time bases is that fewer generalized coordinates need to be computed in order to characterize the complete space–time solution. This is because *both* space *and* time are embedded to the reduced bases, as opposed to just one or the other.¹ This approach is quite new as most of the previous works in the literature propose using parameter- and time-dependent generalized coordinates (i.e., spatial

¹We also note that space-time basis computations are generally more computationally expensive and complicated than usual spatial bases due to memory requirements and implementations.

bases) [24, 37, 38, 39, 40, 41] and very few works use only parameter-dependent generalized coordinates (i.e., space-time bases) [42, 43]. In comparison to these and previous works, the list below summarizes our contributions to the current state-of-the-art detailed in this paper:

- Our proposed method can be considered as non-intrusive model reduction (or data-driven model reduction) and PDE-agnostic which means that one does not need to know (and solve) any underlying *reduced* partial differential equation (PDE) online. The only requirement is that full-order model snapshots are already available (to create space-time bases and train surrogate models).
- We compare various machine learning techniques to approximate the mapping between input parameters and output space-time bases expansion coefficients: multivariate polynomial regression, k-nearest neighbors, random forest and neural network.
- In the offline stage, we collect usual (space-time) state snapshots to build space-time bases and train the machine learning surrogate models. In the online stage, for an arbitrary input parameter we express the space-time solution as linear combinations of those space-time bases and compute the coefficients using the trained surrogate models.
- The space-time basis expansion coefficients only depend on input parameters and *not* on time.
- The proposed method is verified on three benchmark problems: parameterized steady heat conduction PDE, parameterized unsteady heat conduction PDE and parameterized advective-diffusive-reactive problem. Numerical results show that the online computation of machine learning surrogate models is extremely fast and the relative solution error is less than 1% on average.
- We show that while our proposed approach is less accurate than the least-square Petrov-Galerkin (LSPG) model reduction (without hyper-reduction)[44, 45, 46], it is significantly faster.

The paper is structured as follows. Section 2 characterizes the full-order models for both steady and unsteady problems. Section 3 details the proposed projection-based model reduction technique that address both steady (Section 3.1) and unsteady problems (Section 3.2). Section 4 describes four machine learning methods used to construct the mapping between input parameters and the output basis expansion coefficients. Section 5 reports the numerical experiments, and Section 6 concludes the paper.

2 Full-order model

We consider the (high-fidelity) full-order model (FOM) of a dynamical system represented as a parameterized system of ordinary differential equations (ODEs)

$$\mathbf{r}(\mathbf{x}; \boldsymbol{\mu}) := \mathbf{f}(\mathbf{x}, t; \boldsymbol{\mu}) - \dot{\mathbf{x}} = \mathbf{0}, \quad \mathbf{x}(0; \boldsymbol{\mu}) = \mathbf{x}^0(\boldsymbol{\mu}), \quad (2.1)$$

where $t \in [0, T]$ denotes time with final time $T \in \mathbb{R}_+$, and $\mathbf{x} : [0, T] \times \mathcal{D} \rightarrow \mathbb{R}^{N_s}$ denotes the time-dependent, parameterized state as the solution of problem (2.1) for the parameters $\boldsymbol{\mu} \in \mathcal{D}$, and $\mathbf{r} : \mathbb{R}^{N_s} \times \mathcal{D} \rightarrow \mathbb{R}^{N_s}$ is time-continuous residual (trivially zero) at time t . Here, $\mathcal{D} \subseteq \mathbb{R}^{n_\mu}$ is the parameter space, $\mathbf{x}^0 : \mathcal{D} \rightarrow \mathbb{R}^{N_s}$ is the parameterized initial condition, and $\mathbf{f} : \mathbb{R}^{N_s} \times [0, T] \times \mathcal{D} \rightarrow \mathbb{R}^{N_s}$ is the velocity. Differentiation of a variable x with respect to time is denoted by \dot{x} . Dynamical systems such as these may arise from the semidiscretization of a time-dependent PDE model. We refer to Eq. (2.1) as the FOM ODE.

We note that when $\dot{\mathbf{x}}$ vanishes, the FOM model reduces to a steady parameterized system of nonlinear algebraic equations. In such a case, all time-derivatives in the following treatment disappear.

Numerically solving Eq. (2.1) requires a time-discretization method. In this work we use a linear multistep method. A linear k -step method applied to Eq. (2.1) leads to the algebraic system

$$\mathbf{r}^n(\mathbf{x}^n; \boldsymbol{\mu}) = \mathbf{0}, \quad n = 1, \dots, N_t, \quad (2.2)$$

where the time-discrete residual $\mathbf{r}^n : \mathbb{R}^{N_s} \times \mathcal{D} \rightarrow \mathbb{R}^{N_s}$ is defined as

$$\mathbf{r}^n : (\boldsymbol{\xi}; \boldsymbol{\nu}) \mapsto \alpha_0 \boldsymbol{\xi} - \Delta t \beta_0 \mathbf{f}(\boldsymbol{\xi}, t^n; \boldsymbol{\nu}) + \sum_{j=1}^k \alpha_j \mathbf{x}^{n-j} - \Delta t \sum_{j=1}^k \beta_j \mathbf{f}(\mathbf{x}^{n-j}, t^{n-j}; \boldsymbol{\nu}). \quad (2.3)$$

Here, \mathbf{x}^k is the numerical approximation to $\mathbf{x}(k\Delta t; \boldsymbol{\mu})$, $\Delta t \in \mathbb{R}_+$ is the time step, and coefficients α_j and β_j , $j = 0, \dots, k$ with $\sum_{j=0}^k \alpha_j = 0$ define a particular linear multistep scheme. We obtain an implicit time-discretization scheme if $\beta_0 \neq 0$. In this paper we use a uniform time step Δt and a fixed k for each time instance. We refer to Eq. (2.2) as the FOM ODE.

The time-continuous solution field is a function of both space and time. Thus, the full solution lives in the tensor product manifold of both space and time, i.e.,

$$\mathbf{y}(\cdot; \boldsymbol{\mu}) \in \mathbb{R}^{N_s} \otimes \mathcal{H} \quad (2.4)$$

where \mathcal{H} is the set of functions from $\{t^n\}_{n=0}^{N_t}$ to \mathbb{R} . We refer to $\mathbb{R}^{N_s} \otimes \mathcal{H}$ as the ‘FOM trial space’. Let \mathbf{g} be an isomorphic function that ‘unrolls’ time from \mathcal{H} to \mathbb{R}^{N_t} such that

$$\begin{aligned} \mathbf{g} : \mathbf{u} &\mapsto [\mathbf{u}(t^1) \ \cdots \ \mathbf{u}(t^{N_t})] \\ &: \mathbb{R}^p \otimes \mathcal{H} \rightarrow \mathbb{R}^p \otimes \mathbb{R}^{N_t}, \end{aligned} \quad (2.5)$$

where $p \in \mathbb{N}$ is an arbitrary dimension. This yields an equivalent (discrete) representation of the FOM space as

$$\mathbf{g}(\mathbf{y}(\cdot; \boldsymbol{\mu})) = [\mathbf{y}(t^1; \boldsymbol{\mu}) \ \cdots \ \mathbf{y}(t^{N_t}; \boldsymbol{\mu})] \in \mathbb{R}^{N_s} \otimes \mathbb{R}^{N_t}. \quad (2.6)$$

Let us also define a vectorization function which converts the matrix solution to a single column vector

$$\begin{aligned} \mathbf{h} : \mathbf{u} &\mapsto \text{vec}(\mathbf{g}(\mathbf{u})) \\ &: \mathbb{R}^p \otimes \mathcal{H} \rightarrow \mathbb{R}^{pN_t}. \end{aligned} \quad (2.7)$$

3 Projection-based linear model reduction

We now consider applying projection-based model reduction for the full order models presented in Section 2: Section 3.1 addresses steady problems and Section 3.2 addresses unsteady problems.

3.1 Proper orthogonal decomposition for steady problems

We begin by prescribing the subset of the original state space \mathbb{R}^{N_s} on which the ROM techniques will seek approximate solutions. Assume that we have constructed reduced bases $\boldsymbol{\Phi} = [\boldsymbol{\phi}_1, \dots, \boldsymbol{\phi}_p] \in \mathbb{R}_{\star}^{N_s \times p}$ with $p \leq N_s$, where $\mathbb{R}_{\star}^{m \times n}$ denotes the non-compact Stiefel manifold: the set of full-column-rank $m \times n$ real-valued matrices. (We shall describe the popular snapshot-POD approach for constructing such bases later in this section.) We then approximate the solution in the associated p -dimensional trial subspace with

$$\mathbf{x}(\boldsymbol{\mu}) \approx \tilde{\mathbf{x}}(\boldsymbol{\mu}) = \mathbf{x}_{\text{ref}}(\boldsymbol{\mu}) + \sum_{i=1}^p \boldsymbol{\phi}_i \hat{x}_i(\boldsymbol{\mu}) \in \mathbb{R}^{N_s}, \quad (3.1)$$

where $\hat{\mathbf{x}}(\boldsymbol{\mu}) = [\hat{x}_1(\boldsymbol{\mu}), \dots, \hat{x}_p(\boldsymbol{\mu})]^T \in \mathbb{R}^p$ is the generalized/reduced coordinates (or coefficients), $\mathbf{x}_{\text{ref}}(\boldsymbol{\mu})$ is a fixed ‘particular solution’ or also referred in some literature as ‘static correction’. (We refer to [24] for a specific way to compute $\mathbf{x}_{\text{ref}}(\boldsymbol{\mu})$.)

Remark 1. Given the reduced bases $\boldsymbol{\Phi} \in \mathbb{R}^{N_s \times p}$, we approximate the input-output mapping $\boldsymbol{\mu} \in \mathbb{R}^{n_{\boldsymbol{\mu}}} \mapsto \hat{\mathbf{x}}(\boldsymbol{\mu}) \in \mathbb{R}^p$ using different machine learning regression models, such as polynomials, k -nearest neighbors, random forests, and dense neural networks that will be described in Section 4.

Basis construction This section describes how the reduced bases Φ can be constructed assuming that a full-system state-snapshot matrix $\mathbf{X} := [\mathbf{x}(\boldsymbol{\mu}_{\text{train}}^1) - \mathbf{x}_{\text{ref}}(\boldsymbol{\mu}_{\text{train}}^1), \dots, \mathbf{x}(\boldsymbol{\mu}_{\text{train}}^{n_{\text{train}}}) - \mathbf{x}_{\text{ref}}(\boldsymbol{\mu}_{\text{train}}^{n_{\text{train}}})] \in \mathbb{R}^{N_s \times n_{\text{train}}}$ with $\{\boldsymbol{\mu}_{\text{train}}^j\}_{j=1}^{n_{\text{train}}} \subseteq \mathcal{D}$ has been precomputed during an “offline” training stage. Algorithm 1 lists the widely-used proper orthogonal decomposition algorithm that we employ to construct all *spatial* reduced bases in this work. Throughout, $v \in [0, 1]$ is the “energy criterion” used to determine the applied truncation.

Algorithm 1: POD: Proper orthogonal decomposition

Input: Snapshots $\mathbf{X} \in \mathbb{R}^{N_s \times m}$, energy criterion $v \in [0, 1]$

Output: Reduced-basis matrix $\Phi \in \mathbb{R}^{N_s \times p}$ ($p \leq m$)

- 1: Compute (thin) singular value decomposition (SVD): $\mathbf{X} = \mathbf{U}\mathbf{\Sigma}\mathbf{V}^T$,
 - 2: Set $\Phi = [\mathbf{u}_1 \cdots \mathbf{u}_p]$, where $p = \min_{i \in \Gamma(v)} \Gamma(v) := \{i \mid \sum_{j=1}^i \sigma_j^2 / \sum_{k=1}^m \sigma_k^2 \geq v\}$. Here, $\mathbf{U} \equiv [\mathbf{u}_1 \cdots \mathbf{u}_m]$ and $\mathbf{\Sigma} \equiv \text{diag}(\sigma_1, \dots, \sigma_m)$.
-

To compute bases $\Phi \in \mathbb{R}^{N_s \times p}$ for steady problems, we simply execute Algorithm 1 such that $\Phi = \text{POD}(\mathbf{X}, v)$.

3.2 Space-time projection-based model reduction for unsteady problems

As in the previous section, we begin by formulating the reduced basis solution, followed by the construction of the space-time basis. Let $\Phi = [\phi_1, \dots, \phi_p] \in \mathbb{R}_*^{N_s \times n_s}$ represent the spatial basis matrix and $\Psi = [\psi_1, \dots, \psi_k] \in \mathbb{R}_*^{N_t \times n_t}$ be the temporal basis matrix, then each spatiotemporal basis is contained in the span of the tensor product space $\pi := \Phi \otimes \Psi = \{\phi_i \otimes \psi_j\}_{i,j=1}^{n_s, n_t} \in \mathbb{R}^{N_s N_t \times n_{st}}$ where $n_{st} = n_s n_t$. While this tensor product construction of space-time basis is most straightforward, in this paper we have chosen a tailored set of spatiotemporal bases, which is slightly different, but without loss of generality, can be represented in a similar tensor product form.

Following the idea in [43], we seek the approximated numerical solution $\tilde{\mathbf{x}}(\boldsymbol{\mu})$ to reside in an affine space-time trial subspace

$$\tilde{\mathbf{x}}(\boldsymbol{\mu}) = \mathbf{x}_{\text{ref}}(\boldsymbol{\mu}) + \sum_{i=1}^{n_{st}} \boldsymbol{\pi}_i \hat{x}_i(\boldsymbol{\mu}) \in \mathbb{R}^{N_s N_t}, \quad (3.2)$$

where $\hat{x}_i(\boldsymbol{\mu}) \in \mathbb{R}$, $1 \leq i \leq n_{st}$ are the generalized coordinates (or coefficients), $\boldsymbol{\pi}_i \in \mathbb{R}^{N_s N_t}$ are the spatiotemporal bases in $\Phi \otimes \Psi$, and $\mathbf{x}_{\text{ref}}(\boldsymbol{\mu})$ is a reference solution with possible $\boldsymbol{\mu}$ dependence, commonly referred to as the “static correction” or centered solution (over both space and time). In the case where the reference solution is the initial condition, then $\mathbf{x}_{\text{ref}}(\boldsymbol{\mu}) = \mathbf{x}^0(\boldsymbol{\mu}) \otimes \mathbf{1}_{N_t} \in \mathbb{R}^{N_s N_t}$.

Here, the key idea of (3.2) is that the time dependence of the approximated solution is moved from the generalized coordinates to the basis vectors; this enables fewer generalized coordinates to be computed in order to characterize the complete space-time solution. We emphasize again that this is quite new as most of works in literature proposed to use parameter- and time-dependent generalized coordinates (i.e., spatial bases) [24, 37, 38, 39, 40, 41]; and very few works used only parameter-dependent generalized coordinates (i.e., space-time bases) [42, 43].

Remark 2. Given space-time reduced bases $\{\boldsymbol{\pi}_i\}_{i=1}^{n_{st}} \in \mathbb{R}^{N_s N_t}$, we approximate the input-output mapping $\boldsymbol{\mu} \in \mathbb{R}^{n_\mu} \mapsto \hat{\mathbf{x}}(\boldsymbol{\mu}) = [\hat{x}_1(\boldsymbol{\mu}), \dots, \hat{x}_{n_{st}}(\boldsymbol{\mu})]^T \in \mathbb{R}^{n_{st}}$ using different machine learning regression models, such as polynomials, k -nearest neighbors, random forests, and dense neural networks that will be described in Section 4.

Space-time basis construction In order to compute the space-time basis, we evaluate the FOM (2.1) at the set of training parameter instances $\mathbf{D}_{\text{train}} := \{\boldsymbol{\mu}_{\text{train}}^1, \dots, \boldsymbol{\mu}_{\text{train}}^{n_{\text{train}}}\}$ defined by, e.g., uniform sampling, Latin-hypercube sampling, greedy, etc., using a linear multistep method (2.2). This gives us ‘snapshots’ of the solution space $\mathbf{x}(t^j; \boldsymbol{\mu}_{\text{train}}^k) \in \mathbb{R}^{N_s}$, $j \in \mathbb{N}(N_t)$, $k \in \mathbb{N}(n_{\text{train}})$ in both space and time; here $\mathbb{N}(N) := \{1, \dots, N\}$. This data collection procedure is commonly referred to as the ‘offline’ stage in model reduction.

The space-time trial subspace is computed by applying tensor-decomposition techniques to the three-way ‘state tensor’ $\mathcal{X} \in \mathbb{R}^{N_s \times N_t \times n_{\text{train}}}$ with elements

$$\mathcal{X}_{ijk} := x_i(t^j; \boldsymbol{\mu}_{\text{train}}^k) - x_i^{\text{ref}}(\boldsymbol{\mu}_{\text{train}}^k), \quad i \in \mathbb{N}(N_s), \quad j \in \mathbb{N}(N_t), \quad k \in \mathbb{N}(n_{\text{train}}). \quad (3.3)$$

We refer readers to [43] for a complete research of such space-time bases. We expect our resulting ROM be accurate if the solution exhibits separable behavior in space and time.

In order to construct the basis from this three-way tensor, we introduce two different unfoldings of \mathcal{X} . These unfoldings or reshapings allow us to utilize standard matrix decomposition techniques such as PCA (Principal Component Analysis) with simplicity. The mode-1 and mode-2 unfoldings of \mathcal{X} are defined as

$$\mathbf{X}_{(1)} = [\mathbf{X}(\boldsymbol{\mu}_{\text{train}}^1) \quad \dots \quad \mathbf{X}(\boldsymbol{\mu}_{\text{train}}^{n_{\text{train}}})] \in \mathbb{R}^{N_s \times N_t n_{\text{train}}} \quad (3.4)$$

$$\mathbf{X}_{(2)} = [\mathbf{X}^T(\boldsymbol{\mu}_{\text{train}}^1) \quad \dots \quad \mathbf{X}^T(\boldsymbol{\mu}_{\text{train}}^{n_{\text{train}}})] \in \mathbb{R}^{N_t \times N_s n_{\text{train}}}, \quad (3.5)$$

respectively, where we have defined $\mathbf{X}(\boldsymbol{\mu}) := \mathbf{g}(\mathbf{x}(\cdot; \boldsymbol{\mu}) - \mathbf{x}_{\text{ref}}(\boldsymbol{\mu}))$.

In short, $\mathbf{X}_{(1)}$ removes time as a variable by treating time and the parameter space the same, and $\mathbf{X}_{(2)}$ removes the spatial dimension as a variable by treating space and parameter samples the same. In the model-reduction literature, the matrix $\mathbf{X}_{(1)}$ is typically referred to as the ‘global snapshot matrix’; we refer to it in this work as the ‘spatial snapshot matrix’ as its columns comprise snapshots of the spatial solution over time and parameter variation. Similarly, we refer to $\mathbf{X}_{(2)}$ as the ‘temporal snapshot matrix’ as its columns comprise snapshots of the time-evolution of the solution over variation in space and parameter. Now we can begin computing the spatiotemporal basis vectors.

The spatial reduced bases $\boldsymbol{\Phi} = [\phi_1, \dots, \phi_{n_s}] \in \mathbb{R}^{N_s \times n_s}$ is typically computed using proper orthogonal decomposition applied to the spatial snapshot matrix $\mathbf{X}_{(1)}$ by executing Algorithm 1 to obtain $\boldsymbol{\Phi} = \text{POD}(\mathbf{X}_{(1)}, v)$. This produces a basis for the spatial component that is, in a sense, averaged over time. The temporal reduced bases $\boldsymbol{\Psi} = [\psi_1, \dots, \psi_{n_t}] \in \mathbb{R}^{N_t \times n_t}$, can be computed similarly by applying Algorithm 1 on $\mathbf{X}_{(2)}$, i.e., $\boldsymbol{\Psi} = \text{POD}(\mathbf{X}_{(2)}, v)$. Then, spatiotemporal reduced bases can be computed straightforwardly from the Kronecker product $\boldsymbol{\pi} = \boldsymbol{\Phi} \otimes \boldsymbol{\Psi}$.

Alternatively, we propose using the ‘tailored temporal bases’ defined in [43] due to its advantageous capabilities in capturing the time evolution of each individual spatial basis vector. In particular, we use ST-HOSVD (sequentially truncated high-order SVD) [47, 48]. The idea can be summarized as follows. First, for each spatial basis vector ϕ_i we project each space-time snapshot $\mathbf{X}(\boldsymbol{\mu}_{\text{train}}^m)$, $m \in \mathbb{N}(n_{\text{train}})$ onto ϕ_i , $i \in \mathbb{N}(n_s)$. This computation can be performed by a single matrix-vector multiplication to create $\mathbf{X}(\phi_i)_{(2)} = \mathbf{X}_{(2)}\phi_i \in \mathbb{R}^{N_t \times n_{\text{train}}}$. Then, in order to obtain the n_t^i -dimensional tailored temporal bases corresponding to ϕ_i , we simply apply an SVD, as in Algorithm 1, giving us a collection of tailored temporal basis vectors $\boldsymbol{\Psi}^i \in \mathbb{R}^{N_t \times n_t^i}$, where n_t^i may be different for each spatial basis vector ϕ_i . We then repeat this for all n_s spatial basis vectors to get a total of $\sum_{i=1}^{n_s} n_t^i$ temporal basis vectors. Finally, the Kronecker product is implemented corresponding to each spatial basis vector to create resulting spatiotemporal bases $\boldsymbol{\pi} = \{\phi_i \otimes \boldsymbol{\Psi}^i\} \in \mathbb{R}^{N_s N_t \times n_{st}}$, $i \in \mathbb{N}(n_s)$. Detailed implementations are listed in Algorithm 2.

There are several notes for this approach described as follow. First, the maximum dimension of each temporal basis is limited by the number of training-parameter instances, i.e., $n_t^i \leq n_{\text{train}}$, $i \in \mathbb{N}(n_s)$. Second, this approach is less computationally expensive than applying directly SVD on $\mathbf{X}_{(2)}$ above since we shall perform n_s SVD algorithms on $\mathbf{X}(\phi_i)_{(2)} \in \mathbb{R}^{N_t \times n_{\text{train}}}$, while $\mathbf{X}_{(2)} \in \mathbb{R}^{N_t \times N_s n_{\text{train}}}$ and typically $n_s \ll N_s$. Third, Ref. [43] has shown that comparing with other temporal basis approaches, this approach is very efficient since it provides similar accuracy levels but using far fewer degrees of freedom (in the context of GNAT hyper-reduction technique) as each temporal basis vector is tailored to its associated spatial basis vector. Finally this was the approach employed to construct temporal bases in previous works based on forecasting [49, 50].

Algorithm 2: Space-time POD: Space-time proper orthogonal decomposition

Input: Spatial snapshot matrix $\mathbf{X}_{(1)} \in \mathbb{R}^{N_s \times N_t m}$, energy criterion $v \in [0, 1]$

Output: Spatiotemporal basis matrix $\boldsymbol{\pi} \in \mathbb{R}^{N_s N_t \times p n_t^i}$

- 1: Compute (thin) singular value decomposition (SVD) for $\mathbf{X}_{(1)} = \mathbf{U} \boldsymbol{\Sigma} \mathbf{V}^T$.
 - 2: Set $\boldsymbol{\Phi} = [\mathbf{u}_1 \cdots \mathbf{u}_p]$, where $p = \min_{i \in \Gamma(v)} \Gamma(v) := \{i \mid \sum_{j=1}^i \sigma_j^2 / \sum_{k=1}^{N_t m} \sigma_k^2 \geq v\}$. Here, $\mathbf{U} \equiv [\mathbf{u}_1 \cdots \mathbf{u}_{N_t m}]$ and $\boldsymbol{\Sigma} \equiv \text{diag}(\sigma_1, \dots, \sigma_{N_t m})$; $p \leq N_t m$
 - 3: Form $\mathbf{X}_{(2)} = \mathbf{X}_{(1)}^T \in \mathbb{R}^{N_t \times N_s m}$
 - 4: For each \mathbf{u}_i , compute SVD of $\mathbf{X}_{(2)} \cdot \mathbf{u}_i = \mathbf{U}^i \boldsymbol{\Sigma}^i (\mathbf{V}^i)^T$ and set $\boldsymbol{\Psi}^i = [\tilde{\mathbf{u}}_1^i \cdots \tilde{\mathbf{u}}_{n_t^i}^i]$ where $\mathbf{U}^i = [\tilde{\mathbf{u}}_1^i \cdots \tilde{\mathbf{u}}_{n_t^i}^i]$, $i \in \mathbb{N}(p)$; $n_t^i \leq m$
 - 5: For each \mathbf{u}_i , compute Kronecker product $\boldsymbol{\pi}_i = \mathbf{u}_i \otimes \boldsymbol{\Psi}^i$, $i \in \mathbb{N}(p)$
 - 6: Set $\boldsymbol{\pi} = [\boldsymbol{\pi}_1 \cdots \boldsymbol{\pi}_p]$.
-

Note that here we generalize so that the number n_t^i can be adapted for each spatial vector, but for simplicity, we will assume a single n_t for a total of $n_s n_t$ spatiotemporal basis vectors.

4 Machine learning surrogate models

Four different machine learning methods were used to approximate the mappings $\boldsymbol{\mu} \mapsto \hat{\mathbf{x}}(\boldsymbol{\mu})$ in Remark 1 and Remark 2, respectively. This section describes the setup and brief overview of each machine learning method. Specific implementation choices for each modeling approach are given in Section 5.

4.1 Learning problem setup

In general, a surrogate model is constructed for the mapping $\boldsymbol{\alpha}(\boldsymbol{\mu}) : \mathcal{D} \mapsto \mathcal{A}$, e.g., $\boldsymbol{\alpha} \equiv \hat{\mathbf{x}}$ and $\mathcal{A} \subseteq \mathbb{R}^p$ (or $\mathcal{A} \subseteq \mathbb{R}^{n_{st}}$), respectively. The outputs $\boldsymbol{\alpha}(\boldsymbol{\mu})$ are the coefficients defined in Eq. (3.1) or Eq. (3.2) and the inputs are system parameters. In general, let $\boldsymbol{\mu} \in \mathcal{D} \subseteq \mathbb{R}^{n_\mu}$ and $\mathcal{A} \subseteq \mathbb{R}^r$.

Consider the case that we have m snapshots, where each snapshot corresponds to a different input parameter. (Note that for steady problem, a snapshot is a spatial FOM solution while for unsteady problem, a snapshot is a space-time FOM solution. Snapshots correspond to different input parameters.) The input parameters corresponding to each snapshot are collected in the matrix $\mathbf{D} \in \mathbb{R}^{m \times n_\mu}$; while the corresponding basis coefficients for each snapshot are collected in the matrix $\mathbf{A} \in \mathbb{R}^{m \times r}$, respectively. Subsequent sections provide an overview of the four methods used to make predictions. For each of these methods, input and output data \mathbf{D} and \mathbf{A} are divided into training and testing sets denoted by $(\mathbf{D}_{\text{train}}, \mathbf{A}_{\text{train}})$ and $(\mathbf{D}_{\text{test}}, \mathbf{A}_{\text{test}})$, where $m = n_{\text{train}} + n_{\text{test}}$ respectively. The goal is to learn the mapping $\boldsymbol{\alpha} : \mathcal{D} \mapsto \mathcal{A}$ from the training data $(\mathbf{D}_{\text{train}}, \mathbf{A}_{\text{train}})$, and test the performance of the ML methods on $(\mathbf{D}_{\text{test}}, \mathbf{A}_{\text{test}})$.

With the available snapshots data $\mathbf{x}(\boldsymbol{\mu})$ and constructed reduced basis $\boldsymbol{\Phi}$ (or $\boldsymbol{\pi}$, respectively), we can obtain the “best” linear ROM approximations by projecting all FOM solutions onto the reduced bases and then compute associated “best” relative error as: $\forall \boldsymbol{\mu} \in \mathcal{D}$

$$\begin{aligned} \hat{\mathbf{x}}_{\text{best}}(\boldsymbol{\mu}) &= (\boldsymbol{\Phi}^T \boldsymbol{\Phi})^{-1} \boldsymbol{\Phi}^T \mathbf{x}(\boldsymbol{\mu}), \\ \text{Compute } \tilde{\mathbf{x}}_{\text{best}}(\boldsymbol{\mu}) &\text{ from } \hat{\mathbf{x}}_{\text{best}}(\boldsymbol{\mu}) \text{ following Eq. (3.1) or Eq. (3.2),} \\ \varepsilon(\boldsymbol{\mu}) &= \frac{\|\mathbf{x}(\boldsymbol{\mu}) - \tilde{\mathbf{x}}_{\text{best}}(\boldsymbol{\mu})\|}{\|\mathbf{x}(\boldsymbol{\mu})\|}, \end{aligned} \tag{4.1}$$

where $\hat{\mathbf{x}}_{\text{best}}(\boldsymbol{\mu}) \in \mathbb{R}^r$ are the “best” generalized coordinates (in linear ROM sense). The training and testing data is then defined as:

$$\mathbf{D}_{\text{train}} = [\boldsymbol{\mu}_{\text{train}}^1, \dots, \boldsymbol{\mu}_{\text{train}}^{n_{\text{train}}}]^T \in \mathbb{R}^{n_{\text{train}} \times n_\mu}; \quad \mathbf{A}_{\text{train}} = [\hat{\mathbf{x}}_{\text{best}}(\boldsymbol{\mu}_{\text{train}}^1), \dots, \hat{\mathbf{x}}_{\text{best}}(\boldsymbol{\mu}_{\text{train}}^{n_{\text{train}}})]^T \in \mathbb{R}^{n_{\text{train}} \times r}, \tag{4.2}$$

$$\mathbf{D}_{\text{test}} = [\boldsymbol{\mu}_{\text{test}}^1, \dots, \boldsymbol{\mu}_{\text{test}}^{n_{\text{test}}}]^T \in \mathbb{R}^{n_{\text{test}} \times n_\mu}; \quad \mathbf{A}_{\text{test}} = [\hat{\mathbf{x}}_{\text{best}}(\boldsymbol{\mu}_{\text{test}}^1), \dots, \hat{\mathbf{x}}_{\text{best}}(\boldsymbol{\mu}_{\text{test}}^{n_{\text{test}}})]^T \in \mathbb{R}^{n_{\text{test}} \times r}. \tag{4.3}$$

4.2 Polynomial regression

The first model considered is multivariate polynomial regression (MPR), which approximates the outputs (or functions) $\alpha(\mu)$ using a multivariate polynomial expansion and least squares regression. In this paper, we use polynomial functions up to fifth order to define the model. The model for a coefficient $\alpha_l(\mu)$ can be written as

$$\alpha_l(\mu) = b_0 + \sum_{i=1}^{n_\mu} b_i \mu_i + \sum_{i=1}^{n_\mu} \sum_{j=1}^{n_\mu} c_{ij} \mu_i \mu_j + \sum_{i=1}^{n_\mu} \sum_{j=1}^{n_\mu} \sum_{k=1}^{n_\mu} d_{ijk} \mu_i \mu_j \mu_k + \dots, \quad l \in \mathbb{N}(r), \quad (4.4)$$

where b_i , $i = 0, 1, \dots, n_\mu$; c_{ij} , $i, j \in \mathbb{N}(n_\mu)$ and d_{ijk} , $i, j, k \in \mathbb{N}(n_\mu)$ are the coefficients of the approximation model, and μ_i, μ_j, μ_k are components of μ . Note that in this type of expansion, known as a full tensor product grid, the number of basis elements scales like s^{n_μ} where s is the polynomial degree. In the offline/training stage, these unknown coefficients are determined via least squares regression that minimizes the mean squared error between the predicted and actual training outputs. Once these coefficients are determined, in the online/evaluation stage one can quickly compute $\alpha(\mu_{\text{test}})$ for any given μ_{test} . (Note that in all numerical experiments in Section 5, the number of training samples are always larger than number of unknown coefficients assuring that the least square problem is well-defined.)

The largest computational complexity arises from solving the least squares systems, i.e. inverting the $\mathbf{D}_{\text{train}}^T \mathbf{D}_{\text{train}}$ covariance term. The computational complexity depends on n_{train} , n_μ and the degree of the regression polynomials. As shown in Section 5, the polynomial regression model is much cheaper to train and to evaluate than other more complicated ML models (such as neural network or random forest regressors).²

4.3 k-nearest neighbor regression

The k-nearest-neighbors (kNN) model can be interpreted as a localized form of multivariate regression: the approximation is computed over a local set of k training samples that are the closest neighbors of the evaluation point μ in the input space. Due to the local nature of kNN approximations, the resulting models do not provide a global interpretation of the underlying relationship between inputs and outputs. Therefore kNN is an unstructured but flexible scheme, balancing the simplicity of polynomial regression with the flexibility of localized models.

In this paper, we consider a standard implementation of kNN that approximates $\alpha(\mu)$ by averaging the outputs associated with the k nearest neighbors. In the offline stage, a k - d tree partitions the data along each input dimension and can be constructed in $O(n_\mu n_{\text{train}})$ time without explicitly calculating any n_μ -dimensional distances. This also allows fast nearest neighbor searches that have an *average* computational complexity of $O(\log(n_{\text{train}}))$ [51, 52]. In the online stage, the predicted output of the kNN model is the weighted average of the training outputs at each of the neighbors; this is essentially a localized linear regression model.

4.4 Random forest regression

The third model considered is random forest regression, which is an ensemble of decision trees, generally trained via the bagging method (or pasting method) [53]. A decision tree partitions the input domain into many regions and makes local average estimates of the output. This is performed in a top down fashion where the data are recursively partitioned at each node using a greedy algorithm to group similar data together. Each node is assigned a certain split criteria, which aims to make a split that creates similar valued subsets of data. Nodes in the tree continue to split the data into left and right child nodes using a series of logical statements. This process continues until certain stopping criteria are satisfied and nodes cease to split, becoming *leaf* nodes. After the data are partitioned into multiple regions, a piecewise constant

²While this is true for low n_μ , e.g., 2 or 3, the number of basis elements grow exponentially. So, for example, if $n_\mu = 7$ the number of basis elements grow to 78,125! This is why a total order or sparse multi-index is necessary for higher dimensions.

regression model is built. Within each region (i.e., leaf node), a constant function is fit as the average of each value in the region.

Many efficient methods for constructing decision trees are available [54]. Once a tree has been learned, predictions can be made rapidly. Given an input, only simple logic statements are processed to reach a leaf node where an average value is computed to obtain the output. Partitioning the training data along each input dimension has a computational complexity of $O(n_{\mu} n_{\text{train}} \log(n_{\text{train}}))$ to build the tree. If a decision tree is approximately balanced, this allows fast predictions on the order of $O(\log(n_{\text{train}}))$. One of the disadvantages of a random forest regression model is that it is not globally differentiable, as opposed to a polynomial model which is infinitely differentiable.

4.5 Neural network regression

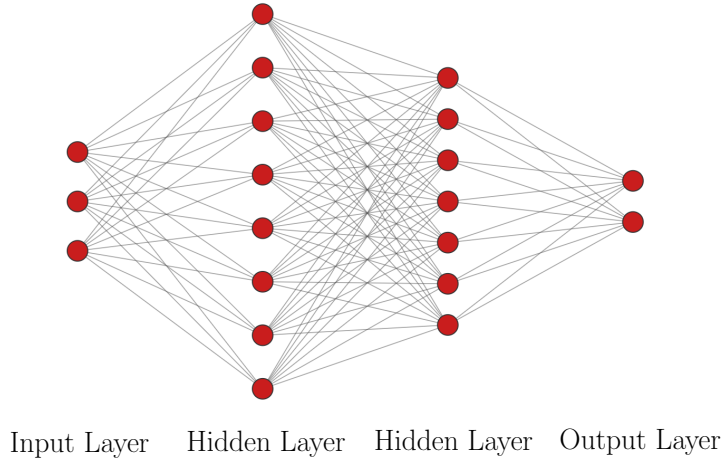


Figure 1: Structure of a neural network with a three dimensional input, two hidden layers and a two dimensional output

The last model considered is a fully connected, feed forward neural network, or multi-layer perceptron model. Neural network models estimate the output $\alpha(\mu)$ at an input μ using weights and biases that are adapted to the data during training. With the use of adaptivity, these models are structured but can achieve great flexibility. A disadvantage of using neural networks is that interpretation of the resulting model may be difficult.

A neural network consists of sequential layers of nodes that define a mapping between an input and an output. The basic structure of a neural network is shown in Figure 1. The first layer of nodes is called the input layer, followed by intermediate hidden layers, and ended with an output layer. The input layer directly receives the input to the model: the number of nodes in the input layer is equal to the number of inputs. Next, in each hidden (i.e., not an input or output) layer l , there are n_l nodes. The i th node in layer l is denoted as η_l^i for $i \in \{1, \dots, n_l\}$. Each node takes an input, evaluates an activation function g , and produces an intermediate output o_l^i , which is used as an input to nodes in the next layer $l + 1$. Every node in a given layer is connected to every node in the following layer (fully connected) and information is passed forward through the network (feed forward). Each of these connections are given a weight w_l^i and a bias b_l^i , which defines the importance and the effect of a particular input to the output [55]. The activation function at each node is a function of $h_l^i = w_l^i o_{l-1}^i + b_l^i$ and thus depends on the input to the node, the weight assigned to the connection to that node and the bias. The output for node η_l^i is determined by evaluating the activation

function $o_i^j = g(h_i^j)$. The last layer is the output layer which produces the final output: the number of nodes in the last layer is equal to the number of output values.

To train a neural network, training inputs $\mathbf{D}_{\text{train}}$ and corresponding training outputs $\mathbf{A}_{\text{train}}$ are provided to the model. The training process iterates forward and backward over the network, adjusting weights and biases to minimize the mean squared error between predicted and actual training outputs [56]. Each pair of forward and backward passes is referred to as an epoch. The computational complexity of training a neural network is approximately linear with the size of the network (nodes and layers), which in turn depends upon the dimension of the input and output, and with the number of epochs, assuming using a smooth activation function [57].

5 Numerical experiments

This section reports numerical experiments that assess the performance of the proposed space-time machine learning ROM (ST-ML-ROM) method on three benchmark problems: a steady heat PDE, an unsteady heat PDE and an advective-diffusive-reactive problem. In particular, the first numerical problem is to check our methods against established results [24], the second problem is to extend to unsteady problems, and the third problem is to check feasibility when there are many spatial/temporal scales and modes are depend nonlinearly on input parameters. We focus on the accuracy and speed of four regression methods (polynomial, kNN, random forest and neural network) and compare the following models:

- **FOM.** This model corresponds to the full-order model, i.e., the solution satisfying Eq. (2.1).
- **ST-ML-ROM.** This model corresponds to data-driven space-time ROMs, i.e., surrogate models constructed via using each ML technique described in sections 4.2–4.5.

For steady and unsteady problems, the accuracy of ROM solutions $\tilde{\mathbf{x}}(\boldsymbol{\mu})$ are measured by computing the ℓ^2 -norm of relative errors:

$$\text{relative error} = \sqrt{\frac{\|\mathbf{x}(\boldsymbol{\mu}) - \tilde{\mathbf{x}}(\boldsymbol{\mu})\|_2^2}{\|\mathbf{x}(\boldsymbol{\mu})\|_2^2}}, \quad (5.1)$$

and

$$\text{relative error} = \sqrt{\sum_{n=1}^{N_t} \|\mathbf{x}^n(\boldsymbol{\mu}) - \tilde{\mathbf{x}}^n(\boldsymbol{\mu})\|_2^2} / \sqrt{\sum_{n=1}^{N_t} \|\mathbf{x}^n(\boldsymbol{\mu})\|_2^2}, \quad (5.2)$$

respectively. All timings are obtained by performing calculations in SKLEARN[58] on a MAC laptop 2.3GHz INTEL Core i9 with 16 GB RAM of memory. Reported timings comprise the average time over specified numbers of repeated runs for offline and online stages of each machine learning method used. We also note that the implementation of all ML methods in this paper are pretty straightforward with standard settings and there is no special treatments such as regularization or any *ad hoc* tuning.

5.1 Parameterized steady heat equation

5.1.1 Full-order model

Table 1: Steady heat equation, parameters of finite element discretization

	Finite element mesh
Number of elements	3600
Number of nodes	3721
Number of degrees of freedom n	3481

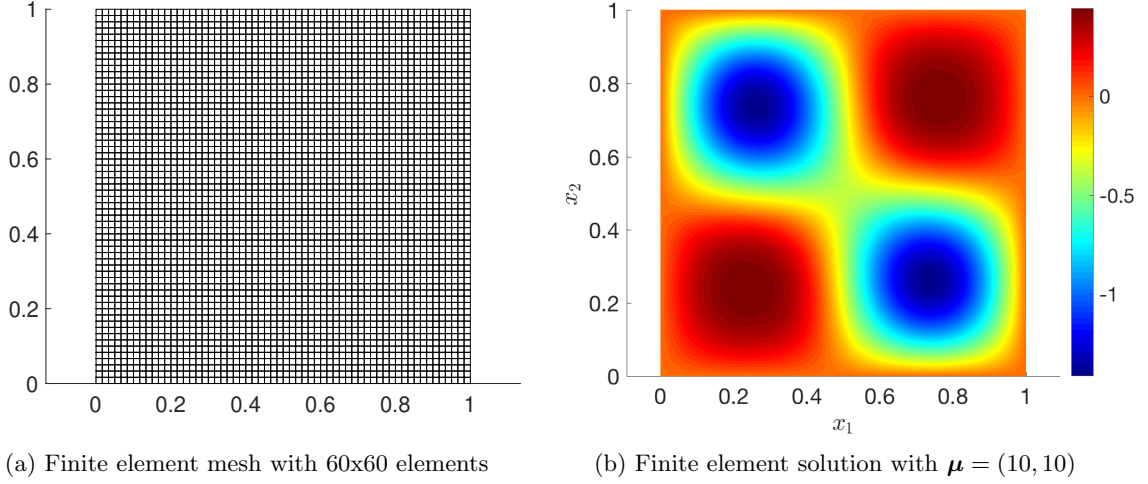


Figure 2: Steady heat equation, finite element mesh and solution.

We first consider the model example introduced in Refs.[59, 13, 46]. This is a parametric nonlinear 2D heat problem which consists of computing $u(\mathbf{x}, \boldsymbol{\mu})$ with $\mathbf{x} \equiv (x_1, x_2) \in \Omega = [0, 1]^2$ and $\boldsymbol{\mu} \equiv (\mu_1, \mu_2) \in \mathcal{D} = [0.01, 10]^2$ and homogeneous Dirichlet boundary condition on $\Gamma \equiv \partial\Omega$ satisfying

$$-\nabla^2 u + \frac{\mu_1}{\mu_2}(e^{\mu_2 u} - 1) = 100 \sin(2\pi x_1) \sin(2\pi x_2). \quad (5.3)$$

This model can be interpreted as a 2D stationary diffusion problem with a nonlinear interior heat source. The resulting solution exhibits a strongly nonlinear dependence on the parameters $\boldsymbol{\mu}$. Note that we use this steady problem to verify all machine learning methods developed earlier (such as the work [24]).

For spatial discretization, we apply the finite-element method using a mesh characterized by 3600 (60x60) bilinear quadrilateral (Q1) elements. Figure 2a depicts the mesh, while Table 1 reports the corresponding discretization parameters. Figure 2b plots the FOM reference solution on the mesh with an input parameter $\boldsymbol{\mu} = (10, 10)$. Applying these finite-element discretizations to Eq. (5.3) leads to a parameterized system of nonlinear algebraic equations of the form (2.1) with $\dot{\mathbf{x}} = 0$.

5.1.2 Model reduction by snapshot-POD

We use Latin Hypercube Sampling with a uniform distribution [60] to generate a total of 300 sample points for the input parameters $\boldsymbol{\mu}$ in \mathcal{D} that is denoted as \mathbf{D} . These 300 sample points are split into 200 training samples ($\mathbf{D}_{\text{train}}$) and 100 testing samples (\mathbf{D}_{test}), where $\mathbf{D}_{\text{train}}$ is used for training purpose and \mathbf{D}_{test} is used for testing purpose. Figure 3a depicts Latin Hypercube Sampling with a uniform distribution, while Figure 3b plots the training and testing samples sets ($\mathbf{D}_{\text{train}}$ and \mathbf{D}_{test}), respectively. We also note that $\mathbf{D} = \mathbf{D}_{\text{train}} \cup \mathbf{D}_{\text{test}}$ and $\mathbf{D}_{\text{train}} \cap \mathbf{D}_{\text{test}} = \emptyset$.

To generate the reduced bases required for the reduced-order models, we solve the FOM (2.1) for all $\boldsymbol{\mu} \in \mathbf{D}_{\text{train}}$, i.e., $\mathbf{X}^{\text{train}} = [\mathbf{x}(\boldsymbol{\mu}_{\text{train}}^1), \dots, \mathbf{x}(\boldsymbol{\mu}_{\text{train}}^{n_{\text{train}}})]$, then feed $\mathbf{X}^{\text{train}}$ to Algorithm 1 to obtain reduced bases. Figure 4 shows the results of Algorithm 1: Figure 4a, 4b plot the singular values and corresponding cumulative energy for spatial SVD. Figure 4b implies that we only need first 5 POD bases to capture more than 99.99% energy of the system, hence we choose $p = 5$ for all computations afterward. Note that we also solve the FOM (2.1) for all $\boldsymbol{\mu} \in \mathbf{D}_{\text{test}}$, i.e., $\mathbf{X}^{\text{test}} = [\mathbf{x}(\boldsymbol{\mu}_{\text{test}}^1), \dots, \mathbf{x}(\boldsymbol{\mu}_{\text{test}}^{n_{\text{test}}})]$ to compute the relative solution error of all proposed ML-ROM techniques later.

Next, we can obtain the “best” linear ROM approximations by projecting all FOM solutions onto the POD bases and then compute associated “best” relative errors following the computation in Eq. (4.1). Figure 5 plots “best” relative solution errors with $\boldsymbol{\mu} \in \mathbf{D}$.

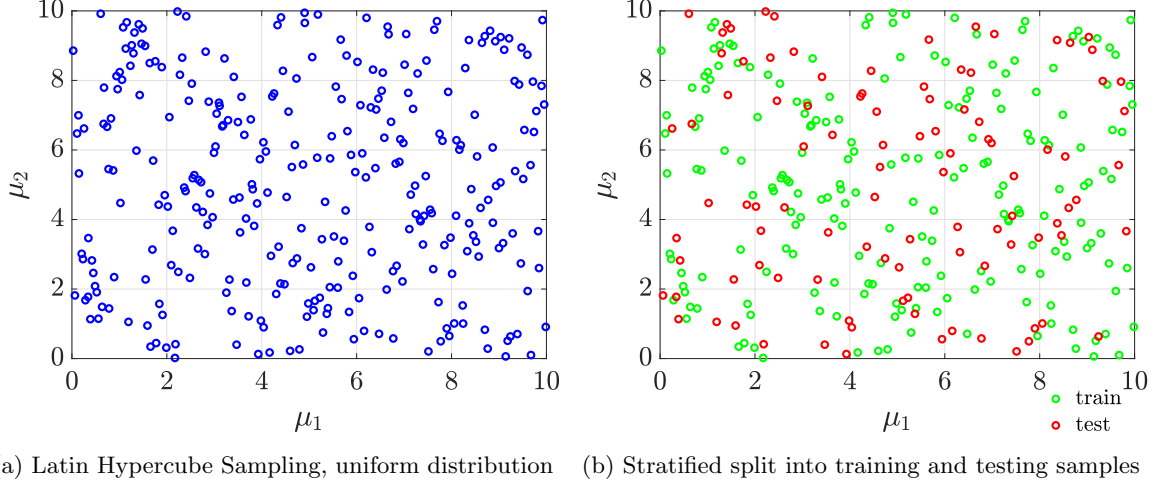


Figure 3: Steady heat equation, sampling the input parameter domain.

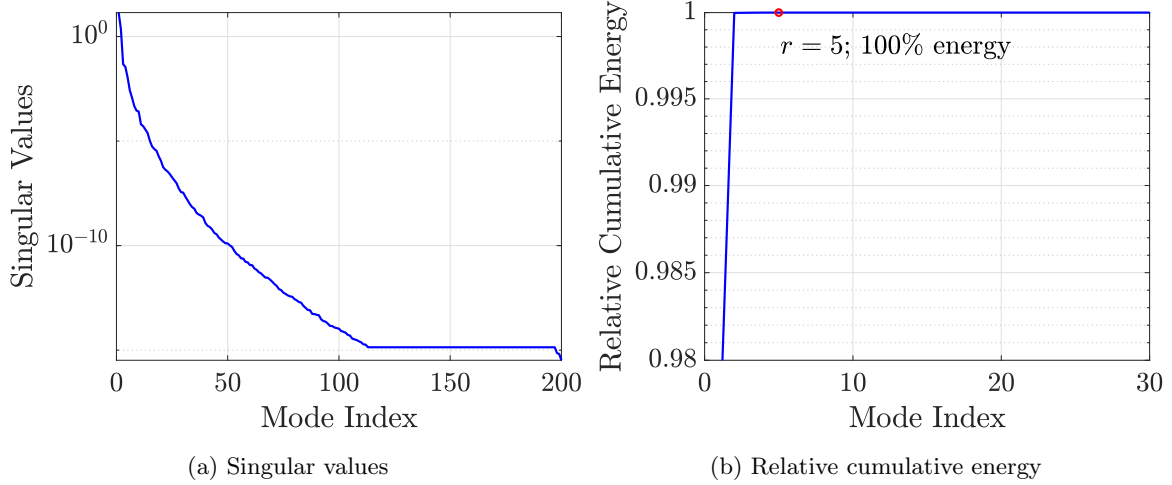


Figure 4: Steady heat equation, singular values decomposition.

We now use the four machine learning techniques described in Section 4 to approximate the mapping $\boldsymbol{\mu} \mapsto \hat{\mathbf{x}}_{\text{best}}(\boldsymbol{\mu})$ by $\boldsymbol{\mu} \mapsto \hat{\mathbf{x}}(\boldsymbol{\mu})$ in the offline (training) stage; then compute the approximated ROM solution Eq. (3.1) and associated relative error Eq. (5.1) in the online (prediction) stage. Note that $\mathbf{D}_{\text{train}}$ is used to build surrogate models and \mathbf{D}_{test} is used to assess the performance (accuracy and speed) of these surrogate models as described in Section 4.1.

5.1.3 ML-ROM: one online computation

We compare the four methods for fixed values of their parameters, and for a single randomly selected online point $\boldsymbol{\mu}_{\text{test}} = (9.0350, 9.2472) \in \mathbf{D}_{\text{test}}$. In particular, we use 2nd order polynomial regressor, kNN regressor with 3 neighbors, random forest regressor with configuration (`max_features=2`, `max_leaf_nodes=16`, `n_estimators=271`) and neural network with configuration (`n_hidden=2`, `n_neurons=50`, `learning_rate=10-3`,

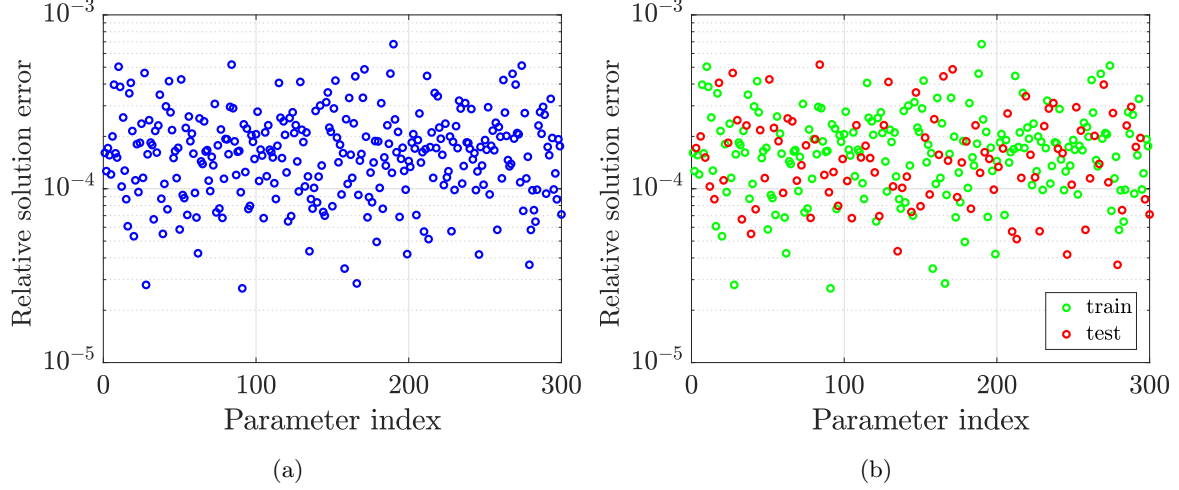


Figure 5: Steady heat equation, “best” relative solution error with $\mu \in D$.

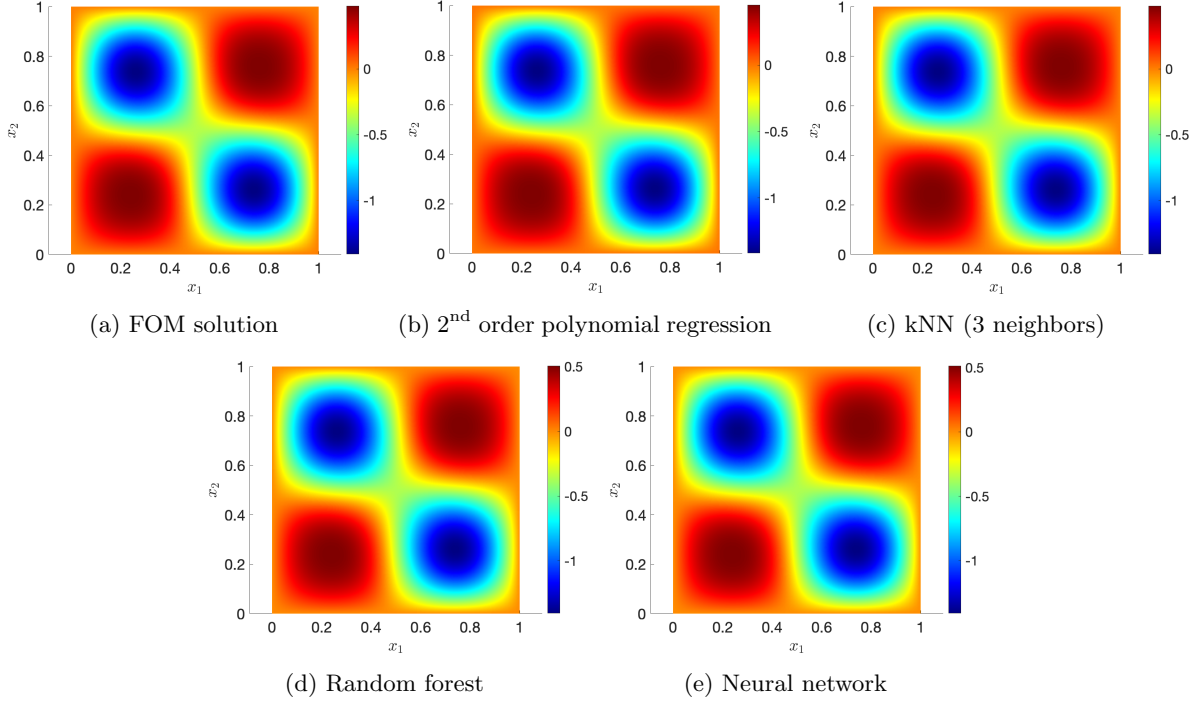


Figure 6: Steady heat equation, FOM solution and ROM predictions using four methods with configurations defined in Table 2 at point $\mu_{\text{test}} = (9.0350, 9.2472) \in D_{\text{test}}$.

`activation=tanh`), respectively³. Note that the configurations and hyper-parameters of these regressors are chosen randomly to check their performance, we will perform a more rigorous parameter study in the next Section 5.1.4.

Table 2 reports the chosen hyper-parameters and associated performance of the methods, while Figure 6

³We refer to [58] for details about these hyper-parameters.

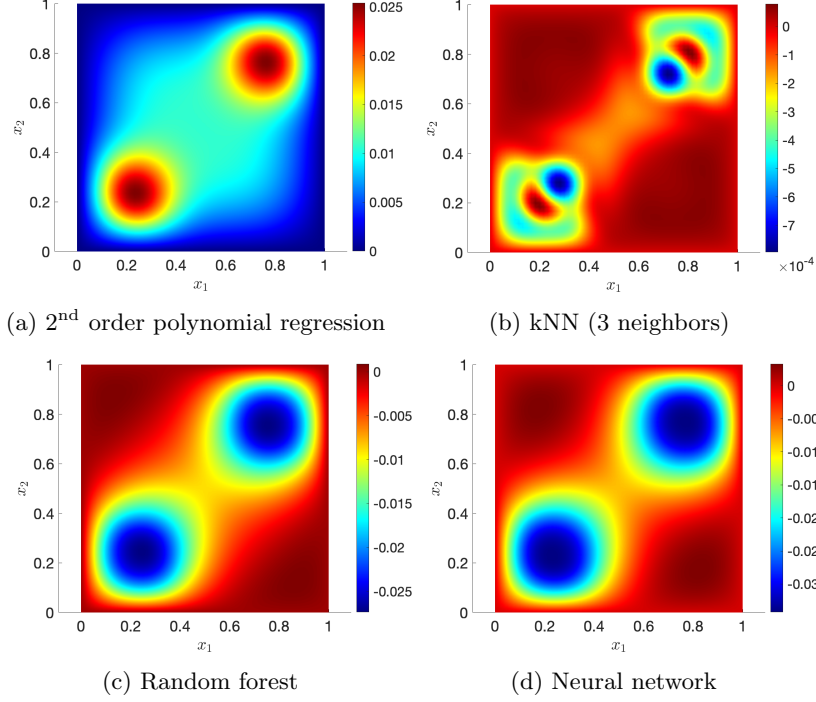


Figure 7: Steady heat equation, solution error using four methods with configurations defined in Table 2 at point $\mu_{\text{test}} = (9.0350, 9.2472) \in \mathcal{D}_{\text{test}}$.

Table 2: Steady heat equation, ML-ROM methods performance at point $\mu_{\text{test}} = (9.0350, 9.2472) \in \mathcal{D}_{\text{test}}$ for one online computation.

method	polynomial regression	kNN	random forest	neural network
configuration	2 nd order	3 neighbors	(max_features=2, max_leaf_nodes=16, n_estimators=271)	(n_hidden=2, n_neurons=50, learning_rate=10 ⁻³ , activation=tanh)
# of ROM bases	5	5	5	5
rel. sol. error	1.7884×10^{-2}	3.21067×10^{-4}	1.9596×10^{-2}	2.4681×10^{-2}

and Figure 7 visualize the ML-ROM solutions and solution errors of all methods, respectively. The results in Table 2 and Figures 6, 7 verify that the proposed methods yield accurate solutions as anticipated [24].

5.1.4 ML-ROM: parameter study

Because assessing a given method's performance for a single instance of its parameters does not lend insight into the model's complete error-cost performance tradeoff, this section subjects each of the proposed ROMs to a parameter study wherein each model parameter is varied within relatively wide ranges. In this spirit, the degree of polynomial regressor will be varied in the range $1 \leq r \leq 5$. For kNN regressor, the number of neighbors will be varied in the range $1 \leq k \leq 19$. For random forest regressor, we first perform a cross-validation randomized search [61] with hyper-parameter limits specified in Table 3. Table 4 reports hyper-parameter values associated with nine *best* configurations of random forest regressors resulting from the

Table 3: Steady heat equation, hyper-parameter ranges of cross-validation randomized search for random forest regressor

Hyper-parameters	Range/Limit
max_features	[1,3]
max_leaf_nodes	[1,300]
n_estimators	[1,500]

Table 4: Steady heat equation, hyper-parameters of nine *best* configurations of random forest regressor

Hyper-parameters	config 1	config 2	config 3	config 4	config 5	config 6	config 7	config 8	config 9
max_features	2	2	2	1	1	2	2	2	1
max_leaf_nodes	16	47	3	7	23	24	38	21	8
n_estimators	271	446	485	21	331	492	386	161	189

Table 5: Steady heat equation, hyper-parameter ranges of cross-validation randomized search for neural network regressor

Hyper-parameters	Range/Limit
n_hidden	{1,2,3,4}
n_neurons	[1,100]
learning_rate	$[10^{-4}, 10^{-1}]$
activation	{relu, tanh, sigmoid}

Table 6: Steady heat equation, hyper-parameters of nine *best* configurations of neural network regressor

Hyper-parameters	config 1	config 2	config 3	config 4	config 5	config 6	config 7	config 8	config 9
n_hidden	2	2	2	4	2	1	1	3	3
n_neurons	79	2	90	39	13	98	17	54	86
learning_rate	1.0260 $\times 10^{-3}$	4.5620 $\times 10^{-3}$	1.0469 $\times 10^{-2}$	1.2136 $\times 10^{-2}$	2.0250 $\times 10^{-3}$	4.0999 $\times 10^{-2}$	1.6280 $\times 10^{-3}$	1.0100 $\times 10^{-4}$	3.6850 $\times 10^{-3}$
activation	tanh	sigmoid	relu	tanh	relu	sigmoid	relu	relu	tanh

Table 7: Steady heat equation, number of repeated runs of offline and online stages for *each* configuration of four regressors

methods	polynomial regressor	kNN regressor	random forest	neural network
offline stage	2000	2000	500	5
online stage	2000	2000	500	1000

randomized search. For neural network regressor, we also perform first a cross-validation randomized search [61] with hyper-parameter ranges specified in Table 5. Table 6 reports hyper-parameter values associated with nine *best* configurations of neural network regressors after the randomized search.

We then investigate the accuracy of these configurations by computing their relative solution errors for all $\mu \in \mathbf{D}_{\text{test}}$. The computational results are shown in Figure 8. In particular, the relative errors are presented in the form of data boxes where on each box the median, 25th, 75th percentiles, most extreme data points and outliers are all shown together. For reference, the “best” relative error defined in (4.1) is also added to Figure 8 as the lowermost data box. Figure 8 shows that the proposed methods yield accurate solutions and reasonable error levels for engineering problems.

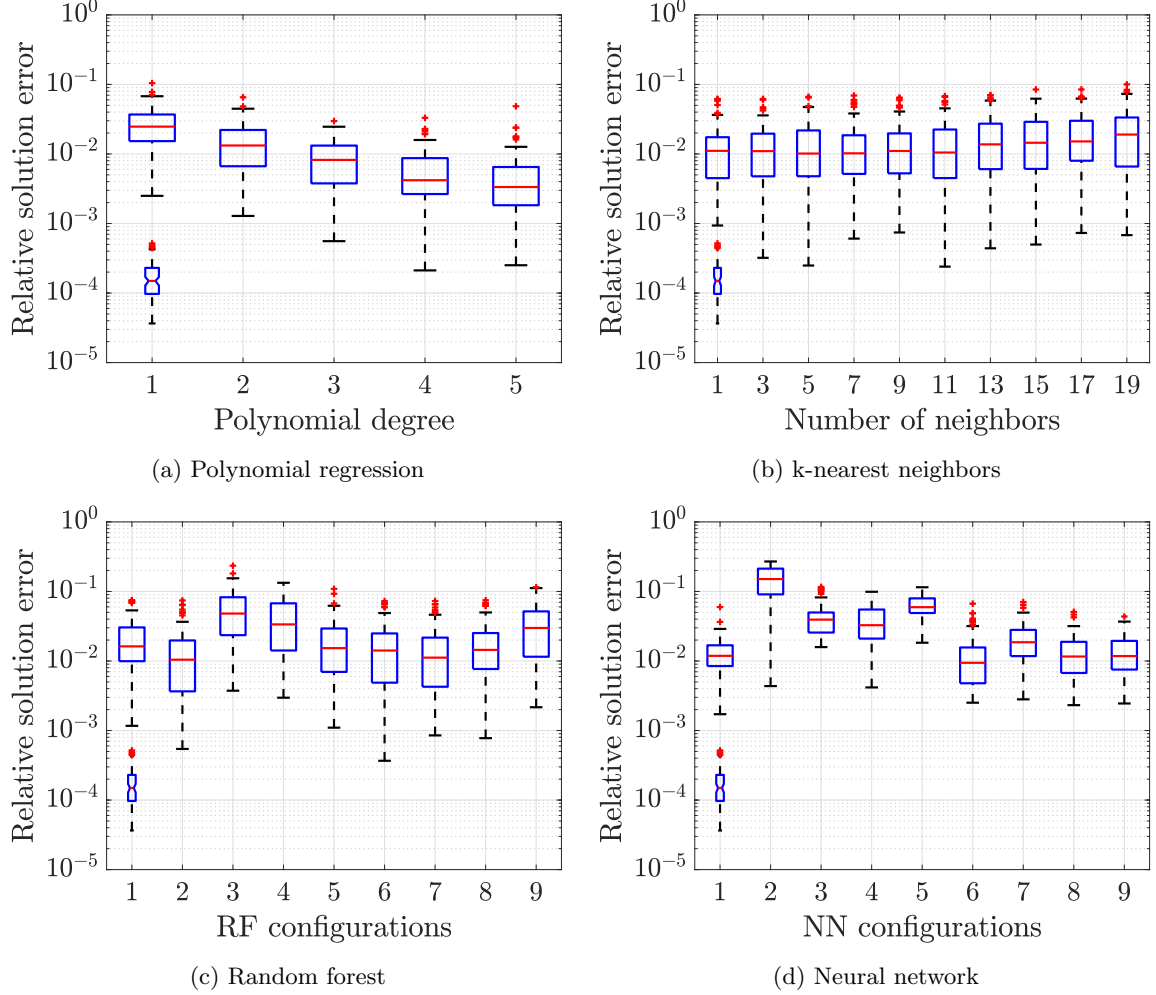
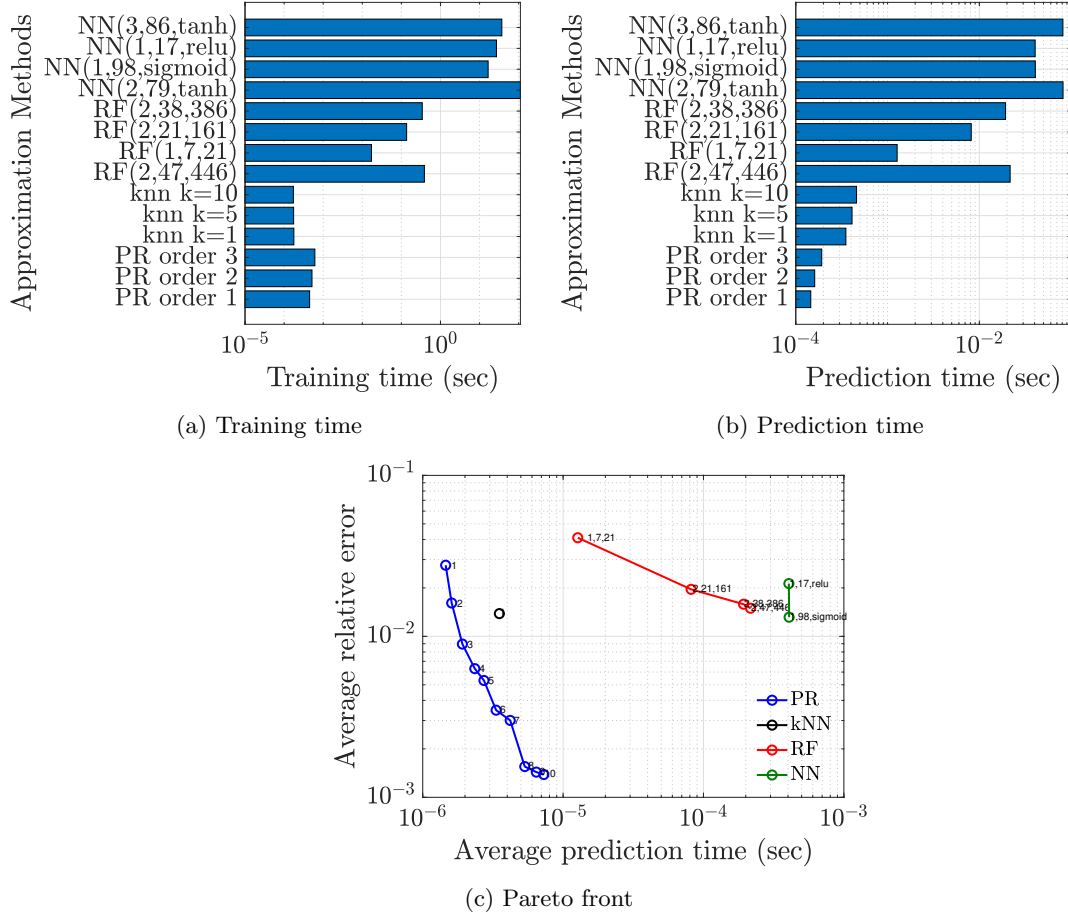


Figure 8: Steady heat equation, relative solution error with $\mu \in \mathbf{D}_{\text{test}}$. The lowermost box is for “best” relative error defined in Eq. (4.1), all upper boxes for ML-ROM using four machine learning techniques. (On each data box, the central red mark indicates the median, the bottom and top blue edges indicate the 25th and 75th percentiles. The whiskers extend to the most extreme data points not considered outliers, and the outliers are plotted by red plus symbols.)

We also examine the computational time of the considered configurations. To quantify the computation time, the offline and online stages of *each* configuration of the four methods are repeated many times and the reported time is averaged from that of these repeated runs. Table 7 lists the number of repeated runs mentioned previously. We emphasize that the reported time only measures the time to compute $\mu \rightarrow \hat{x}(\mu)$, and does not include $\hat{x}(\mu) \rightarrow \tilde{x}(\mu)$ as the step $\hat{x}(\mu) \rightarrow \tilde{x}(\mu)$ is the same for all regressors. Figure 9a and 9b report the training time and prediction time of some configurations of four regressors. In general, we observe that neural network takes much more time to train and predict than the other three techniques.

From the results in Figures 8 and 9b, we construct a Pareto front to characterize the error–cost for each method. This Pareto front is characterized by the method hyper-parameters that minimize the competing objectives of relative error and computational time. Figure 9c reports the Pareto fronts of the four methods considered. From Figure 9c, we observe a very similar trend to that in the work [24] in which simple ML techniques (such as polynomial, kNN and random forest regressors) outperform complex ML ones (such as



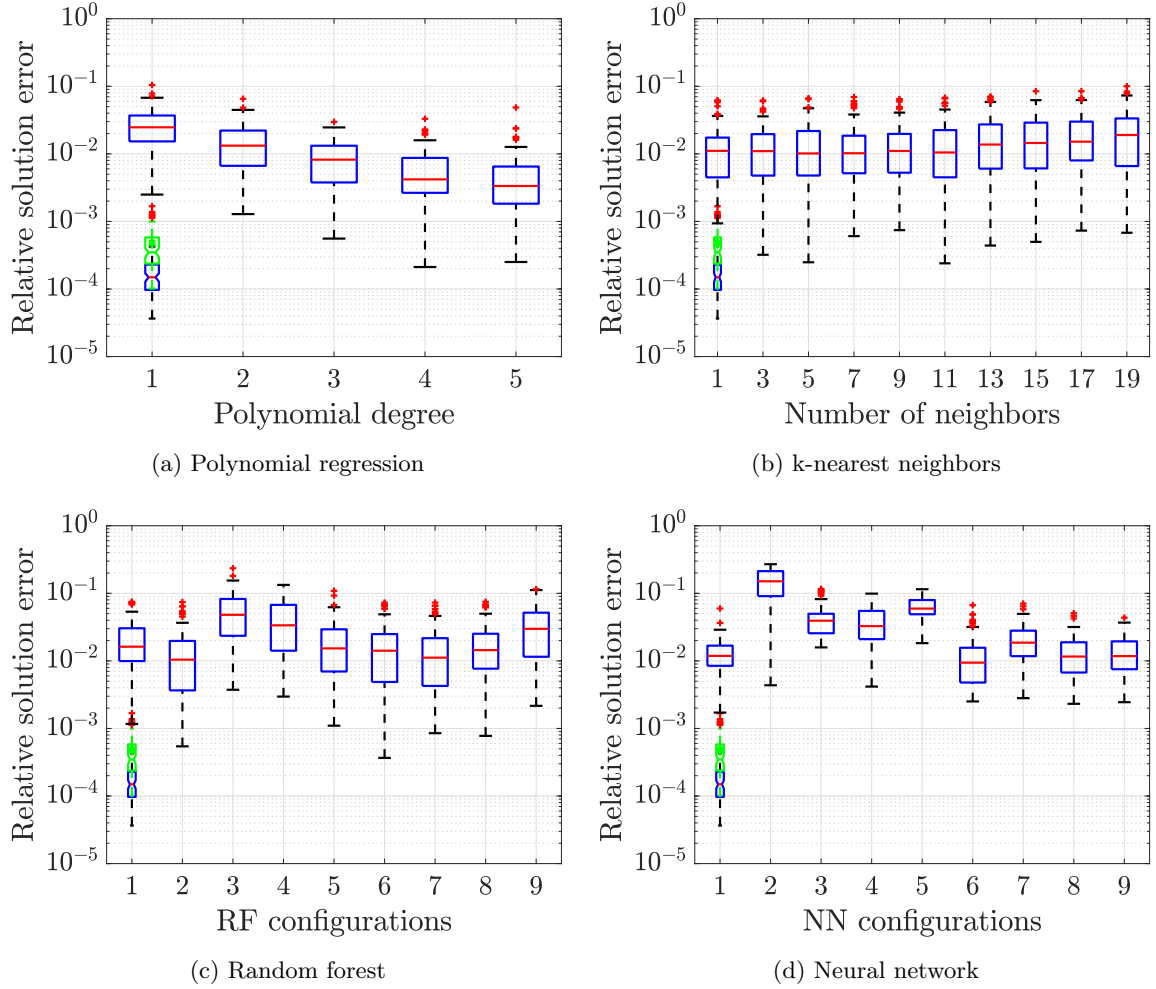


Figure 10: Steady heat equation, relative solution error with $\mu \in \mathcal{D}_{\text{test}}$. The lowermost box is for “best” relative error defined in 4.1, the middle box is for LSPG-ROM (green color) [44], and all upper boxes for ML-ROM using four machine learning techniques.

(without hyper-reduction) is much higher than that of our proposed methods⁴.

5.2 Parameterized unsteady heat equation

5.2.1 Full-order model

We now consider the model example introduced in Refs. [59, 13]. This is a parametric nonlinear 2D unsteady heat problem which consists of computing $u(\mathbf{x}, t, \mu)$ with $\mathbf{x} \equiv (x_1, x_2) \in \Omega = [0, 1]^2$, $t \in [0, T]$ with $T = 2$ and $\mu \equiv (\mu_1, \mu_2) \in \mathcal{D} = [0.01, 10]^2$ and homogeneous Dirichlet boundary condition on $\Gamma \equiv \partial\Omega$, such that:

$$\rho \frac{\partial u}{\partial t} - \nabla^2 u + \frac{\mu_1}{\mu_2} (e^{\mu_2 u} - 1) = \rho b(t) \sin(2\pi x_1) \sin(2\pi x_2), \quad (5.4)$$

⁴Note that LSPG-ROM (without hyper-dimension) needs to solve a nonlinear optimization problem in the online stage where computational cost still depends full-order model dimension, while our proposed methods has computational cost completely independent of FOM dimension.

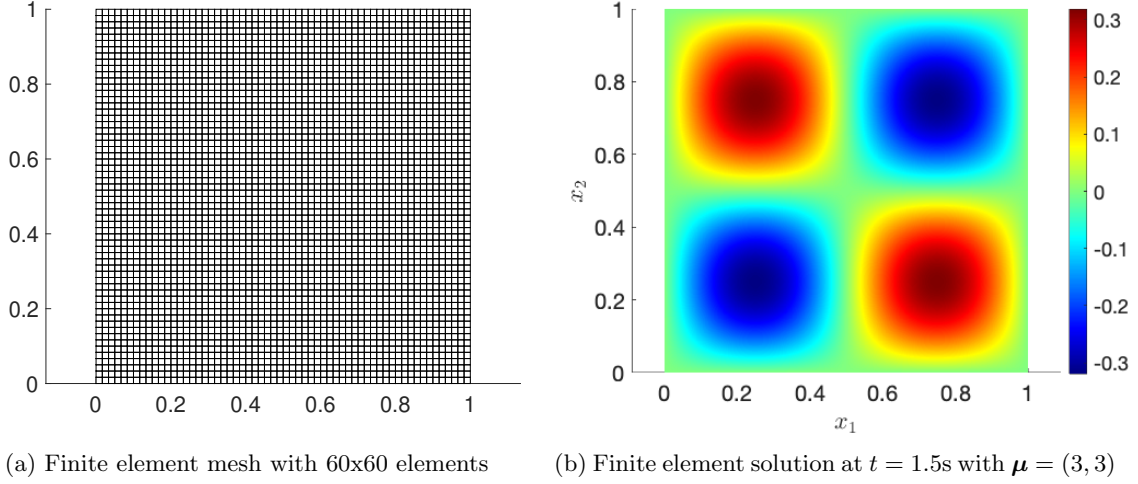


Figure 11: Unsteady heat equation, finite element mesh and solution.

where $\rho = 10^4$ is a constant, $b = \sin(2\pi t)$ is the control input. This model can be interpreted as a 2D dynamically diffusion problem with a nonlinear interior heat source density. It presents nonlinear dependence of the solution with respect the input parameter μ .

For spatial discretization, we use a finite element mesh with 3600 (60×60) bilinear quadrilateral (Q1) elements, which results in a system of parameterized ODEs of the form (2.1). The same Table 1 also reports the spatial discretization parameters used for this model. For time discretization, we employ the first order backward Euler scheme which is a linear multistep method characterized by $k(t^n) = 1$, $\alpha_0^n = \beta_0^n = 1$, $\alpha_1^n = -1$, $\beta_1^n = 0$, $n \in \mathbb{N}(N_t)$ in (2.3). We use a uniform time step $\Delta t = 8 \times 10^{-3}$, leading to $N_t = 250$ time instances. Figure 11a depicts the mesh, while Figure 11b plots the FOM reference solution at time instance $t = 1.5$ s with $\mu = (3, 3)$, respectively.

5.2.2 Model reduction with space-time bases

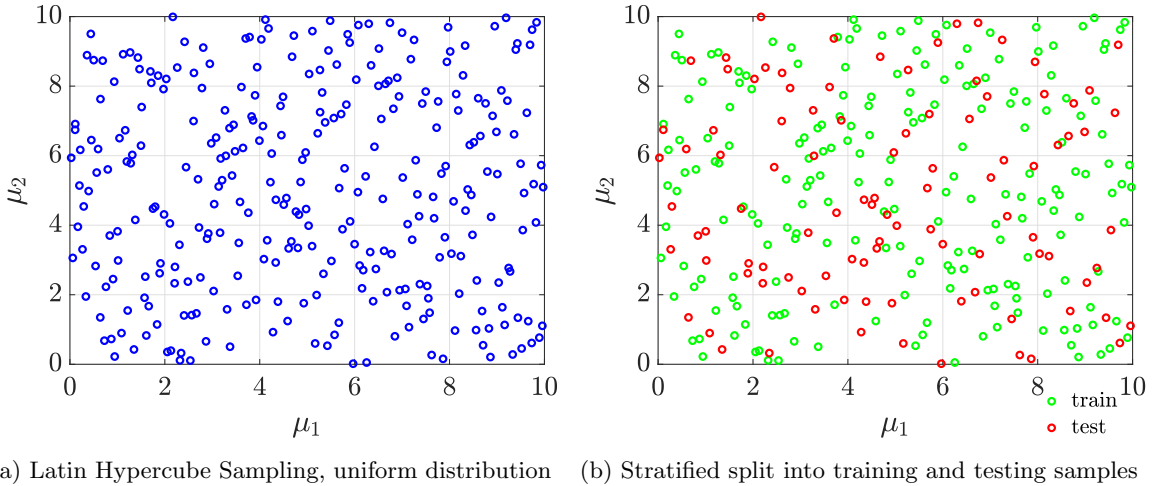


Figure 12: Unsteady heat equation, sampling the input parameter domain.

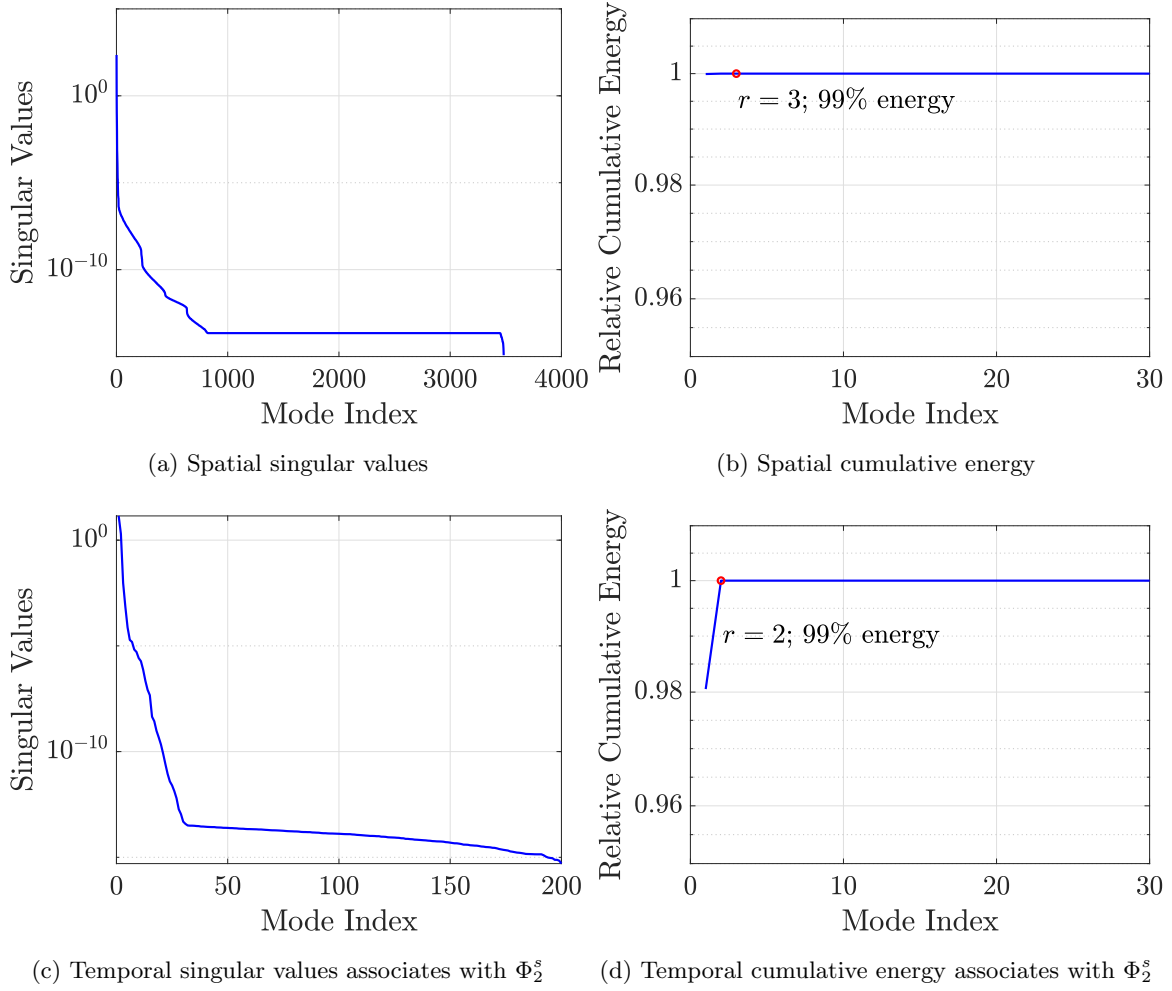


Figure 13: Unsteady heat equation, singular values decomposition.

Similar to section 5.1.2, we use Latin Hypercube Sampling with a uniform distribution [60] to generate a total of 300 sample points for the input parameter μ in \mathcal{D} that is denoted as \mathbf{D} . These 300 sample points are split into 200 training samples ($\mathbf{D}_{\text{train}}$) and 100 testing samples (\mathbf{D}_{test}), where $\mathbf{D}_{\text{train}}$ is used for training purposes and \mathbf{D}_{test} is used for testing purposes. Figure 12a depicts Latin Hypercube Sampling with a uniform distribution, while Figure 12b plots the training and testing samples sets ($\mathbf{D}_{\text{train}}$ and \mathbf{D}_{test}), respectively. We also note that $\mathbf{D} = \mathbf{D}_{\text{train}} \cup \mathbf{D}_{\text{test}}$ and $\mathbf{D}_{\text{train}} \cap \mathbf{D}_{\text{test}} = \emptyset$.

To generate the space-time reduced bases required for the reduced-order models, we solve the FOM (2.2) for all $\mu \in \mathbf{D}_{\text{train}}$, i.e., $\mathbf{X}^{\text{train}} = [\mathbf{x}(t^n, \mu_{\text{train}}^1), \dots, \mathbf{x}(t^n, \mu_{\text{train}}^{n_{\text{train}}})]$, $n \in \mathbb{N}(N_t)$ then feed $\mathbf{X}^{\text{train}}$ to Algorithm 2 to obtain the space-time bases. Figure 13 shows the results after performing this step. In particular, Figure 13a, 13b present singular values and cumulative energy for spatial SVD, while Figure 13c and 13d plot singular values and cumulative energy for temporal SVD associated with Φ_2^s . From Figures 13b and 13d, we choose $n_s = 3$ spatial bases, $n_t = 2$ temporal bases, hence $n_{st} = n_s n_t = 6$ space-time reduced bases for all computations afterward. Again, we also solve the FOM (2.2) for all $\mu \in \mathbf{D}_{\text{test}}$, i.e., $\mathbf{X}^{\text{test}} = [\mathbf{x}(t^n, \mu_{\text{test}}^1), \dots, \mathbf{x}(t^n, \mu_{\text{test}}^{n_{\text{test}}})]$, $n \in \mathbb{N}(N_t)$ to compute the relative solution error of all proposed ML-ROM techniques. We finally obtain the “best” linear ROM approximations by projecting all space-time FOM solutions onto the space-time bases and then compute associated “best” relative errors following Eq. (4.1).

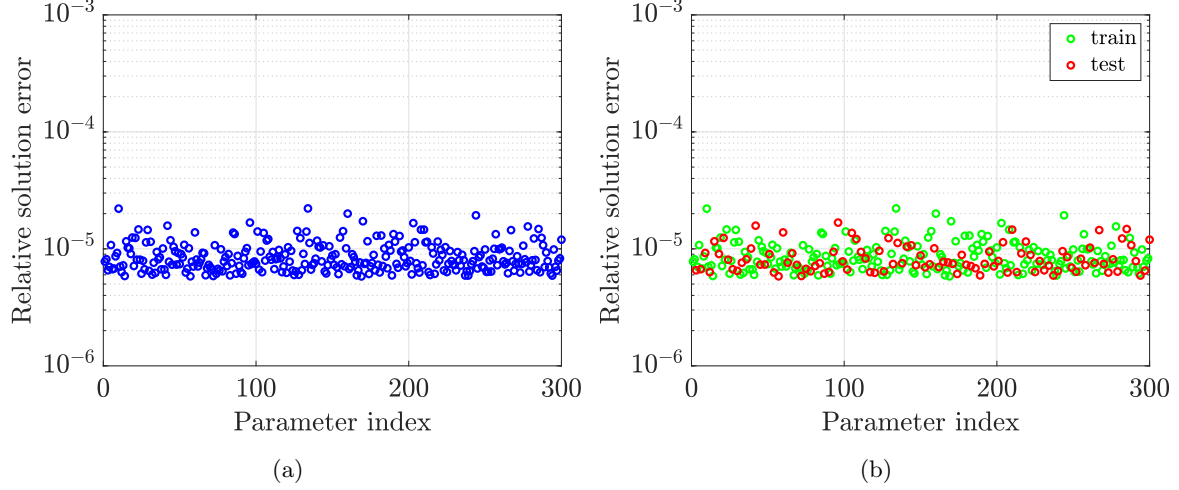


Figure 14: Unsteady heat equation, “best” relative error for $\mu \in \mathcal{D}^{\text{total}}$ with $n_s = 3$, $n_t = 2$, $p = n_s n_t = 6$.

Figure 14 plots “best” relative solution errors with $\mu \in \mathcal{D}$ using n_s , n_t and n_{st} chosen above.

We now use the four machine learning techniques described in Section 4 to approximate the mapping $\mu \rightarrow \hat{x}(\mu)$ in the offline (training) stage; then compute the approximated ROM solution Eq. (3.2) and associated relative error Eq. (5.2) in the online (prediction) stage. Note again that $\mathcal{D}_{\text{train}}$ is used to build surrogate models and $\mathcal{D}_{\text{test}}$ is used to assess the performance (accuracy and speed) of these surrogate models.

5.2.3 ST-ML-ROM: one online computation

Table 8: Unsteady heat equation, ST-ML-ROM methods performance at point $\mu_{\text{test}} = (9.6289, 7.2334) \in \mathcal{D}_{\text{test}}$ for one online computation.

method	polynomial regression	kNN	random forest	neural network
configuration	2 nd order	3 neighbors	(<code>max_features=2</code> , <code>max_leaf_nodes=44</code> , <code>n_estimators=162</code>)	(<code>n_hidden=4</code> , <code>n_neurons=75</code> , <code>learning_rate=3.74 × 10⁻⁴</code> , <code>activation=sigmoid</code>)
# of ROM bases	6	6	6	6
rel. sol. error	5.5048×10^{-5}	9.3391×10^{-5}	1.0323×10^{-4}	6.6496×10^{-4}

We now compare the four methods for fixed values of their parameters, and for a single randomly selected online point $\mu_{\text{test}} = (9.6289, 7.2334) \in \mathcal{D}_{\text{test}}$. In particular, we use 2nd order polynomial regressor, kNN regressor with 3 neighbors, random forest regressor with configuration (`max_features=2`, `max_leaf_nodes=44`, `n_estimators=162`) and neural network with configuration (`n_hidden=4`, `n_neurons=75`, `learning_rate=3.74 × 10-4`, `activation=sigmoid`), respectively. Note that the configurations and hyper-parameters of these regressors are chosen randomly to check their performance, we will perform a more rigorous parameter study in the next Section 5.2.4.

Table 8 reports the chosen hyper-parameters and associated performance of the methods, while Figure 15 and Figure 16 visualize the ST-ML-ROM solutions and solution errors of all methods at time instance $t = 1.6\text{s}$, respectively. The results on Table 8 and Figures 15, 16 verify that the proposed methods yield very accurate solutions.

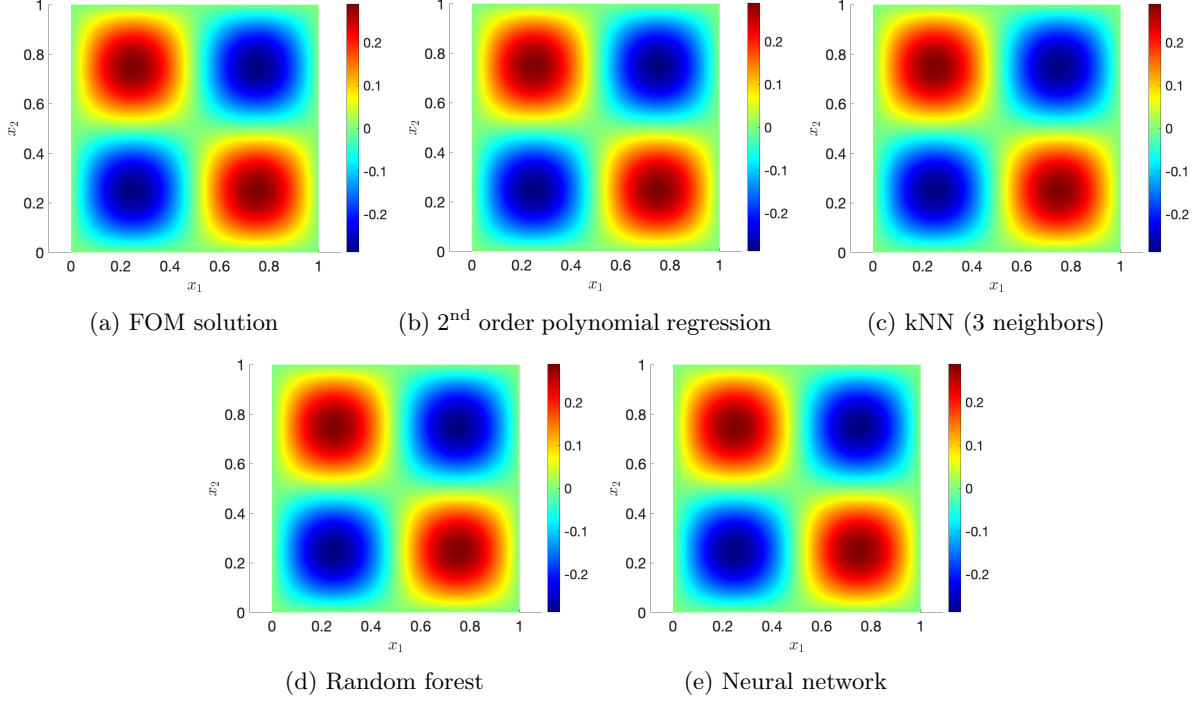


Figure 15: Unsteady heat equation, solution visualization using four methods with configurations specified in Table 8 at time $t = 1.6\text{s}$, $\mu_{\text{test}} = (9.6289, 7.2334) \in \mathcal{D}_{\text{test}}$.

5.2.4 ST-ML-ROM: parameter study and comparison with space-time LSPG-ROM

Table 9: Unsteady heat equation, hyper-parameters of nine *best* configurations of random forest regressor

Hyper-parameters	config 1	config 2	config 3	config 4	config 5	config 6	config 7	config 8	config 9
<code>max_features</code>	2	1	2	2	2	2	2	1	1
<code>max_leaf_nodes</code>	264	167	49	106	44	22	2	88	135
<code>n_estimators</code>	431	274	475	260	162	253	390	373	21

Table 10: Unsteady heat equation, hyper-parameters of nine *best* configurations of neural network regressor

Hyper-parameters	config 1	config 2	config 3	config 4	config 5	config 6	config 7	config 8	config 9
<code>n_hidden</code>	4	3	2	2	4	1	1	1	4
<code>n_neurons</code>	99	43	67	79	75	28	30	67	71
<code>learning_rate</code>	3.4607 $\times 10^{-2}$	1.1950 $\times 10^{-3}$	1.6230 $\times 10^{-3}$	2.9250 $\times 10^{-3}$	3.7400 $\times 10^{-4}$	1.1100 $\times 10^{-4}$	1.1920 $\times 10^{-3}$	4.4430 $\times 10^{-3}$	1.4800 $\times 10^{-4}$
<code>activation</code>	<code>sigmoid</code>	<code>tanh</code>	<code>tanh</code>	<code>sigmoid</code>	<code>sigmoid</code>	<code>tanh</code>	<code>sigmoid</code>	<code>tanh</code>	<code>sigmoid</code>

We again compare the performance of the ROM methods across a wide variation of all method parameters. In particular, the degree of polynomial regressor will be varied in the range $1 \leq r \leq 5$. For kNN regressor, the number of neighbors will be varied in the range $1 \leq k \leq 19$. For random forest and neural network regressors, we employ the same approach as described in Section 5.1.4 to find their *several* optimal configurations.

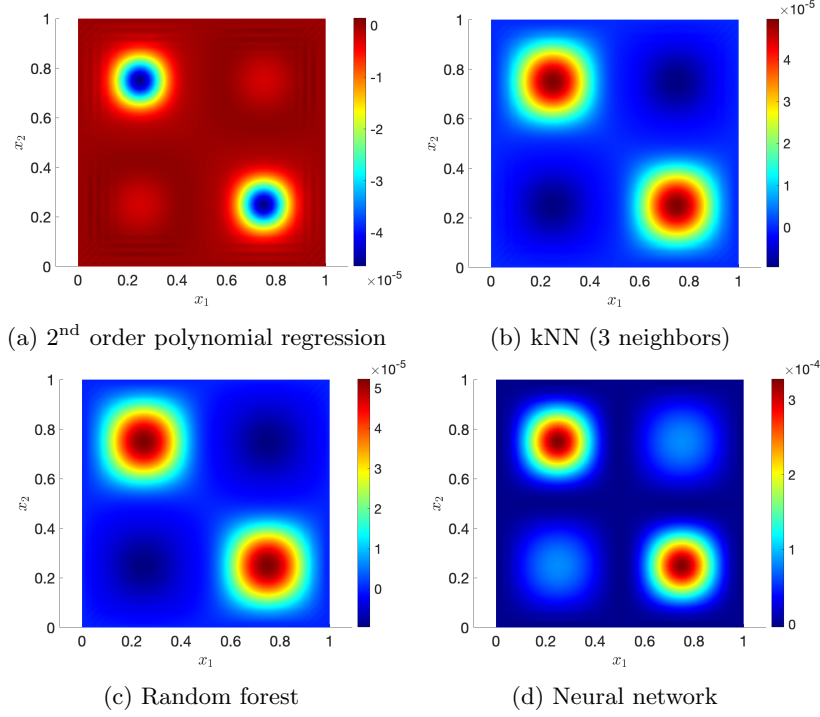


Figure 16: Unsteady heat equation, solution error using four methods with configurations defined in Table 8 at time $t = 1.6\text{s}$, $\mu_{\text{test}} = (9.6289, 7.2334) \in \mathcal{D}_{\text{test}}$.

Since the input-output mapping of this problem ($\mathbb{R}^2 \rightarrow \mathbb{R}^6$) is very similar to that of the previous problem in Section 5.1 ($\mathbb{R}^2 \rightarrow \mathbb{R}^5$), we use the same randomized search ranges for hyper-parameters of random forest and neural network regressors as specified in Tables 3 and 5, respectively. Tables 9 and 10 report hyper-parameter values associated with nine *best* configurations of random forest and neural network regressors resulting from the corresponding cross-validation randomized searches.

We then investigate the accuracy of these configurations by computing their relative solution errors together with the relative solution errors of the space-time LSPG-ROM method [43] and “best” relative error (4.1) for all $\mu \in \mathcal{D}_{\text{test}}$. Figure 17 reports all these relative solution errors. We observe a similarity between Figure 17 and Figure 10 that is the space-time LSPG-ROM provides very accurate solutions that are close to the “best” possible linear ROM solutions; and the space-time LSPG-ROM solutions are *slightly* more accurate than our proposed methods. Again, we also note that the computational cost of space-time LSPG-ROM (without hyper-reduction) is much higher than that of our proposed methods (see Section 5.1.5).

The computational time of the considered configurations are also examined. We apply the same procedure described in Section 5.1.4 to measure computational times; the same Table 7 lists the number of repeated offline and online runs. Figure 18a and Figure 18b report the training time and Pareto front for online predictions, respectively. Again, Figure 18b shows a very similar trend to Figure 9c in which simple ML techniques (such as polynomial, kNN and random forest regressors) outperform complex ML ones (neural network) in terms of accuracy and computational cost for this problem.

5.2.5 Results with 75% training data

We investigate the effect of the amount of training data on computational results. In particular, within training data set $\mathcal{D}_{\text{train}}$, we pick a random nonstratified partition [62] that has 75% size of $\mathcal{D}^{\text{train}}$ to train all ML models, then evaluate the accuracy of these models similarly to Section 5.2.4 above. Figure 19 reports the relative solution errors together with the “best” relative error (4.1) for all $\mu \in \mathcal{D}^{\text{test}}$. Comparing Figure 19

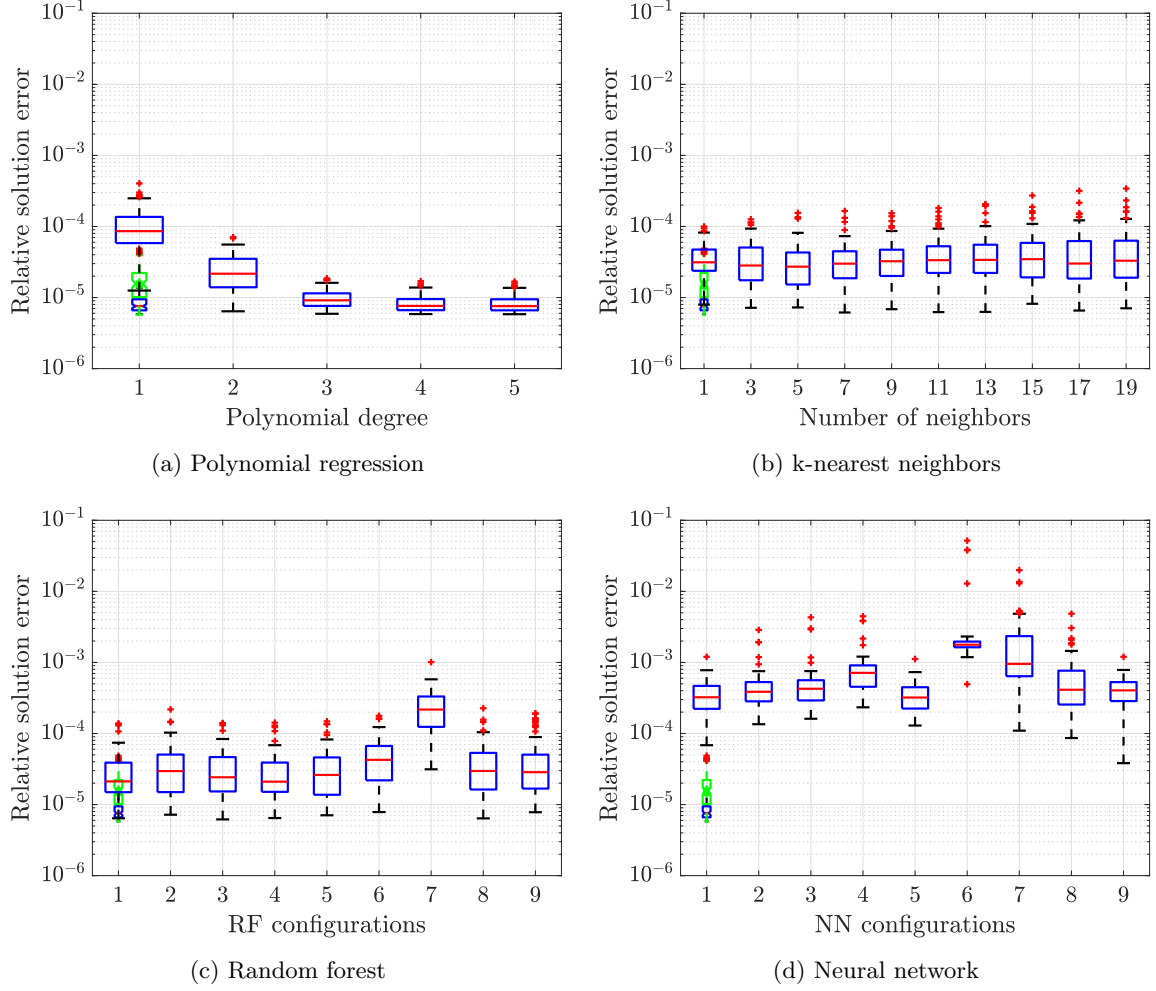


Figure 17: Unsteady heat equation, relative solution error with $\boldsymbol{\mu} \in \mathbf{D}_{\text{test}}$. The lowermost box is for “best” relative error defined in Eq. (4.1), the middle box is for space-time LSPG-ROM (green color) [43], and all upper boxes for ST-ML-ROM using four machine learning techniques.

and Figure 17 shows that all ML algorithms still work well and provide accurate solutions even when using only 75% training data. (It is generally obvious that using much less training data will have adverse effect on the performance of ML algorithms.)

5.3 Parameterized advective-diffusive-reactive system

5.3.1 Full-order model

We now consider an advective-diffusive-reactive system modeled on the premixed combustion of a $\text{H}_2 - \text{O}_2$ mixture at constant pressure. The governing equation system is:

$$\frac{\partial \mathbf{w}(\vec{x}, t; \boldsymbol{\mu})}{\partial t} = \nabla \cdot (\kappa \nabla \mathbf{w}(\vec{x}, t; \boldsymbol{\mu})) - \mathbf{v} \cdot \nabla \mathbf{w}(\vec{x}, t; \boldsymbol{\mu}) + \mathbf{q}(\mathbf{w}(\vec{x}, t; \boldsymbol{\mu}); \boldsymbol{\mu}) \quad \text{in } \Omega \times \mathcal{D} \times [0, T], \quad (5.5)$$

where ∇ is the spatial gradient, κ is the molecular diffusivity, \mathbf{v} is the velocity field, and

$$\mathbf{w}(\vec{x}, t; \boldsymbol{\mu}) \equiv [w_T(\vec{x}, t; \boldsymbol{\mu}), w_{\text{H}_2}(\vec{x}, t; \boldsymbol{\mu}), w_{\text{O}_2}(\vec{x}, t; \boldsymbol{\mu}), w_{\text{H}_2\text{O}}(\vec{x}, t; \boldsymbol{\mu})]^T \in \mathbb{R}^4$$

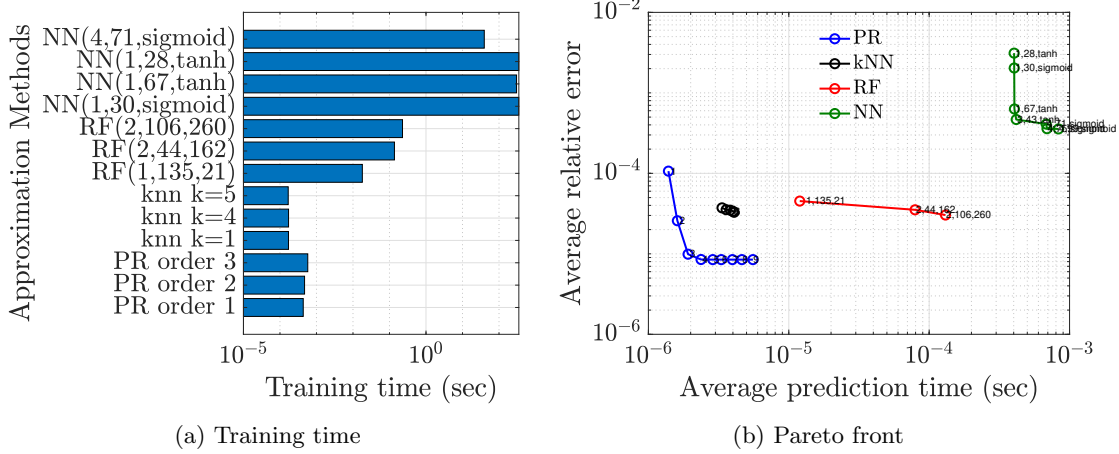


Figure 18: Unsteady heat equation, training time and Pareto front of four ST-ML-ROM techniques: PR=Polynomial Regression, kNN=k-nearest neighbor, RF=Random Forest and NN=Neural Network.

denotes the state vector containing the temperature $w_T(\vec{x}, t; \boldsymbol{\mu})$ and the mass fractions of chemical species H_2 , O_2 , and H_2O , i.e., $w_i(\vec{x}, t; \boldsymbol{\mu})$ for $i \in \{\text{H}_2, \text{O}_2, \text{H}_2\text{O}\}$. The Arrhenius reaction source term $\mathbf{q}(\mathbf{w}(\vec{x}, t; \boldsymbol{\mu}); \boldsymbol{\mu}) \equiv [q_T(\mathbf{w}; \boldsymbol{\mu}), q_{\text{H}_2}(\mathbf{w}; \boldsymbol{\mu}), q_{\text{O}_2}(\mathbf{w}; \boldsymbol{\mu}), q_{\text{H}_2\text{O}}(\mathbf{w}; \boldsymbol{\mu})]^T$ is

$$q_T(\mathbf{w}; \boldsymbol{\mu}) = Q q_{\text{H}_2\text{O}}(\mathbf{w}; \boldsymbol{\mu})$$

$$q_i(\mathbf{w}; \boldsymbol{\mu}) = -\nu_i \left(\frac{W_i}{\rho} \right) \left(\frac{\rho w_{\text{H}_2}}{W_{\text{H}_2}} \right)^{\nu_{\text{H}_2}} \left(\frac{\rho w_{\text{O}_2}}{W_{\text{O}_2}} \right)^{\nu_{\text{O}_2}} A \exp \left(-\frac{E}{R w_T} \right), \quad i \in \{\text{H}_2, \text{O}_2, \text{H}_2\text{O}\},$$

where $(\nu_{\text{H}_2}, \nu_{\text{O}_2}, \nu_{\text{H}_2\text{O}}) = (2, 1, -2)$ are the stoichiometric coefficients, $(W_{\text{H}_2}, W_{\text{O}_2}, W_{\text{H}_2\text{O}}) = (2.016, 31.9, 18)$ are the molecular weights with units $\text{g} \cdot \text{mol}^{-1}$, $\rho = 1.39 \times 10^{-3} \text{ g} \cdot \text{cm}^{-3}$ is the density of the mixture, $R = 8.314 \text{ J} \cdot \text{mol}^{-1} \cdot \text{K}^{-1}$ is the universal gas constant, and $Q = 9800 \text{ K}$ captures the heat of the reaction. The $n_{\boldsymbol{\mu}} = 2$ uncertain parameters are $\boldsymbol{\mu} = (A, \kappa)$, the pre-exponential factor A and the molecular diffusivity. The parameter domain is set to $\mathcal{D} = [2.3375 \times 10^{12}, 6.5 \times 10^{12}] \times [1, 4]$. We define a divergence-free constant velocity field with $\mathbf{v} = [50 \text{ cm} \cdot \text{s}^{-1}, 0]^T$, the activation energy $E = 7.0 \times 10^3$ and the final time is $T = 0.04 \text{ s}$, respectively.

Figure 20a shows the geometry of the spatial domain. At the inflow boundary Γ_2 , Dirichlet boundary conditions $w_{\text{H}_2} = 0.0282$, $w_{\text{O}_2} = 0.2259$ and $w_{\text{H}_2\text{O}} = 0$ are imposed for the mass fractions and $w_T = 950 \text{ K}$ for the temperature. On boundaries Γ_1 and Γ_3 , homogeneous Dirichlet boundary conditions exist for mass fractions, and temperature $w_T = 300 \text{ K}$ is set. On Γ_4, Γ_5 , and Γ_6 , we impose homogeneous Neumann conditions on the temperature and mass fractions. For initial conditions, we use $w_T = 300 \text{ K}$ and $w_{\text{H}_2} = w_{\text{O}_2} = w_{\text{H}_2\text{O}} = 0$.

Eq. (5.5) is solved on a 65×32 finite-difference mesh (see Fig. 20b). A second-order backward difference formula ($k = 2$, $\alpha_0 = 1$, $\alpha_1 = -\frac{4}{3}$, $\alpha_2 = \frac{1}{3}$, $\beta_0 = \frac{2}{3}$, and $\beta_1 = \beta_2 = 0$) is used for temporal discretization. These result in a nonlinear system of the form of Eq. (2.3) with $n = 8192$ degrees of freedom; $\Delta t = 2 \times 10^{-4}$ which implies $N_t = 200$ time instances to solve the problem.

5.3.2 Model reduction with space-time bases

We again use Latin Hypercube Sampling with uniform distribution to generate a total of 400 sample points for the input parameter $\boldsymbol{\mu}$ in \mathcal{D} that is denoted as \mathbf{D} . These 400 sample points are split into 320 training samples ($\mathbf{D}_{\text{train}}$) and 80 testing samples (\mathbf{D}_{test}), where $\mathbf{D}_{\text{train}}$ is used for training purpose and \mathbf{D}_{test} is used for testing purpose. Within $\mathbf{D}_{\text{train}}$, we use only first 150 points to build space-time bases due to implementation

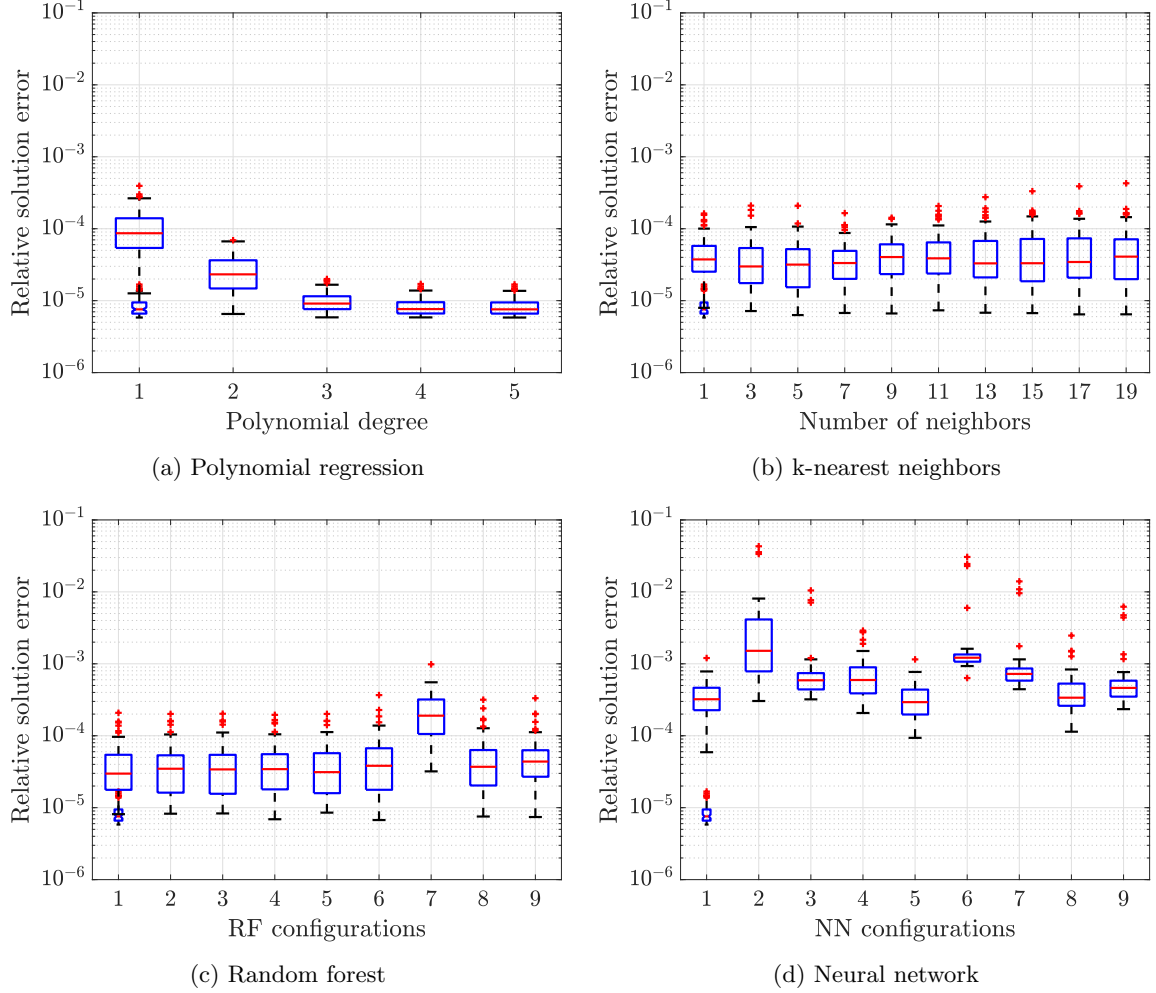


Figure 19: Unsteady heat equation, relative solution error with $\mu \in \mathbf{D}_{\text{test}}$. The lowermost box is for “best” relative error defined in (4.1), and all upper boxes for ST-ML-ROM using four machine learning techniques with 75% training data.

issues⁵. Figure 21a depicts the training and testing samples sets, while Figure 21b plots the training samples points (within $\mathbf{D}_{\text{train}}$) used to build space-time bases, respectively. Note that $\mathbf{D} = \mathbf{D}_{\text{train}} \cup \mathbf{D}_{\text{test}}$ and $\mathbf{D}_{\text{train}} \cap \mathbf{D}_{\text{test}} = \emptyset$.

To generate the space-time reduced bases required for the reduced-order models, we solve the FOM (2.2) for all $\mu \in \mathbf{D}_{\text{train}}$, i.e., $\mathbf{X}^{\text{train}} = [\mathbf{x}(t^n, \mu_{\text{train}}^1), \dots, \mathbf{x}(t^n, \mu_{\text{train}}^{n_{\text{train}}})]$, $n \in \mathbb{N}(N_t)$ then feed $\mathbf{X}^{\text{train}}$ to Algorithm 2 to obtain the space-time bases. Figure 22 shows the results after performing this step: Figure 22a, 22b present singular values and cumulative energy for spatial SVD, while Figure 22c and 22d plot singular values and cumulative energy for temporal SVD associated with Φ_2^s . Based on Figures 22b, 22d and some trial-error experiments, we choose $n_s = 20$ spatial bases, $n_t = 3$ temporal bases, hence $n_{st} = n_s n_t = 60$ space-time reduced bases for all computations afterward.

Again, we also solve the FOM (2.2) for all $\mu \in \mathbf{D}_{\text{test}}$, i.e., $\mathbf{X}^{\text{test}} = [\mathbf{x}(t^n, \mu_{\text{test}}^1), \dots, \mathbf{x}(t^n, \mu_{\text{test}}^{n_{\text{test}}})]$, $n \in \mathbb{N}(N_t)$ to compute the relative solution error of all proposed ST-ML-ROM techniques. We finally obtain the

⁵Note that space-time implementation for this problem is more expensive than the previous example in Section 5.2 in terms of cost and memory requirements due to pretty high number of spatial degrees of freedom $N_s=8192$ and stronger nonlinearity.

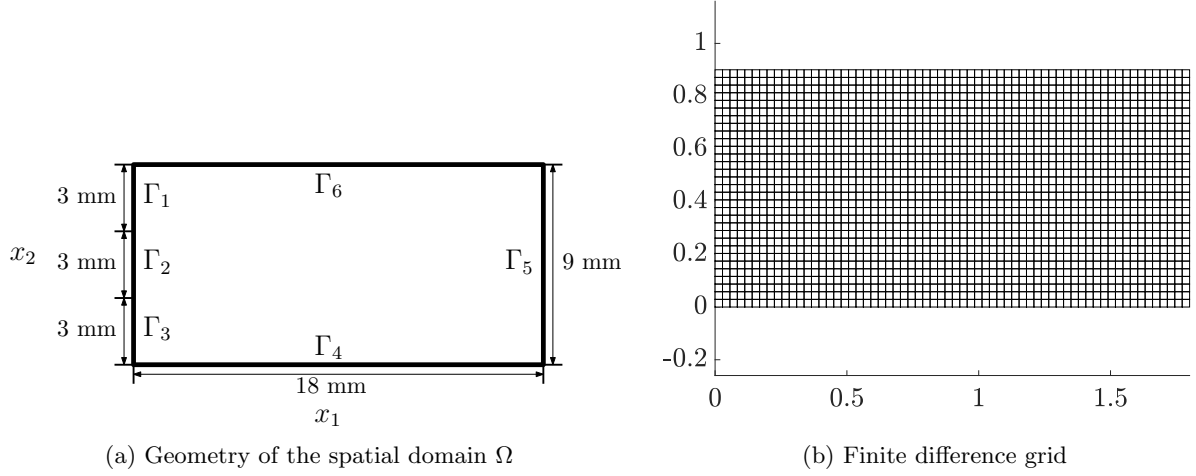


Figure 20: Reacting flow, geometry and finite difference grid.

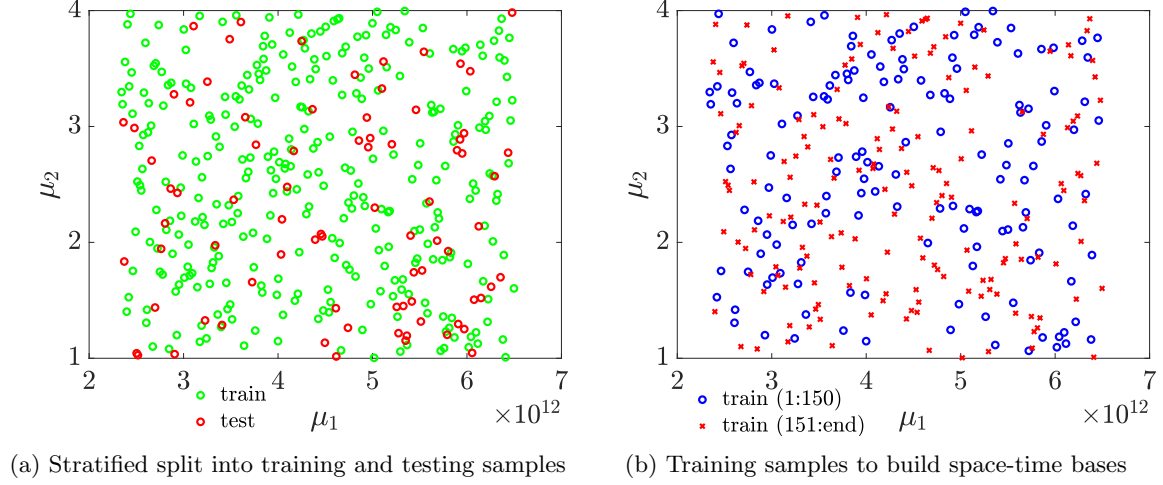


Figure 21: Reacting flow, sampling the input parameter domain.

“best” linear ROM approximations by projecting all space-time FOM solutions onto the space-time bases and then compute associated “best” relative errors following Eq. (4.1). Figure 23 plots “best” relative solution errors with $\boldsymbol{\mu} \in \mathcal{D}$ using n_s , n_t and n_{st} chosen above.

We then build the surrogate models (using four machine learning techniques described in Section 4) for the mapping $\boldsymbol{\mu} \rightarrow \hat{\mathbf{x}}(\boldsymbol{\mu})$. The surrogate models are built in the offline (training) stage using data in $\mathcal{D}_{\text{train}}$; and their performance (accuracy and speed) are evaluated in the online (prediction) stage using data in $\mathcal{D}_{\text{test}}$, respectively.

5.3.3 ST-ML-ROM: one online computation

We now compare the four methods for fixed values of their parameters, and for a single randomly selected online point $\boldsymbol{\mu}_{\text{test}} = (5.9315 \times 10^{12}, 3.5416) \in \mathcal{D}_{\text{test}}$. In particular, we use 2nd order polynomial regressor, kNN regressor with 3 neighbors, random forest regressor with configuration (`max_leaf_nodes`=116, `n_estimators`=81) and neural network with configuration (`n_hidden`=10, `n_neurons`=19, `learning_rate`=1.27×

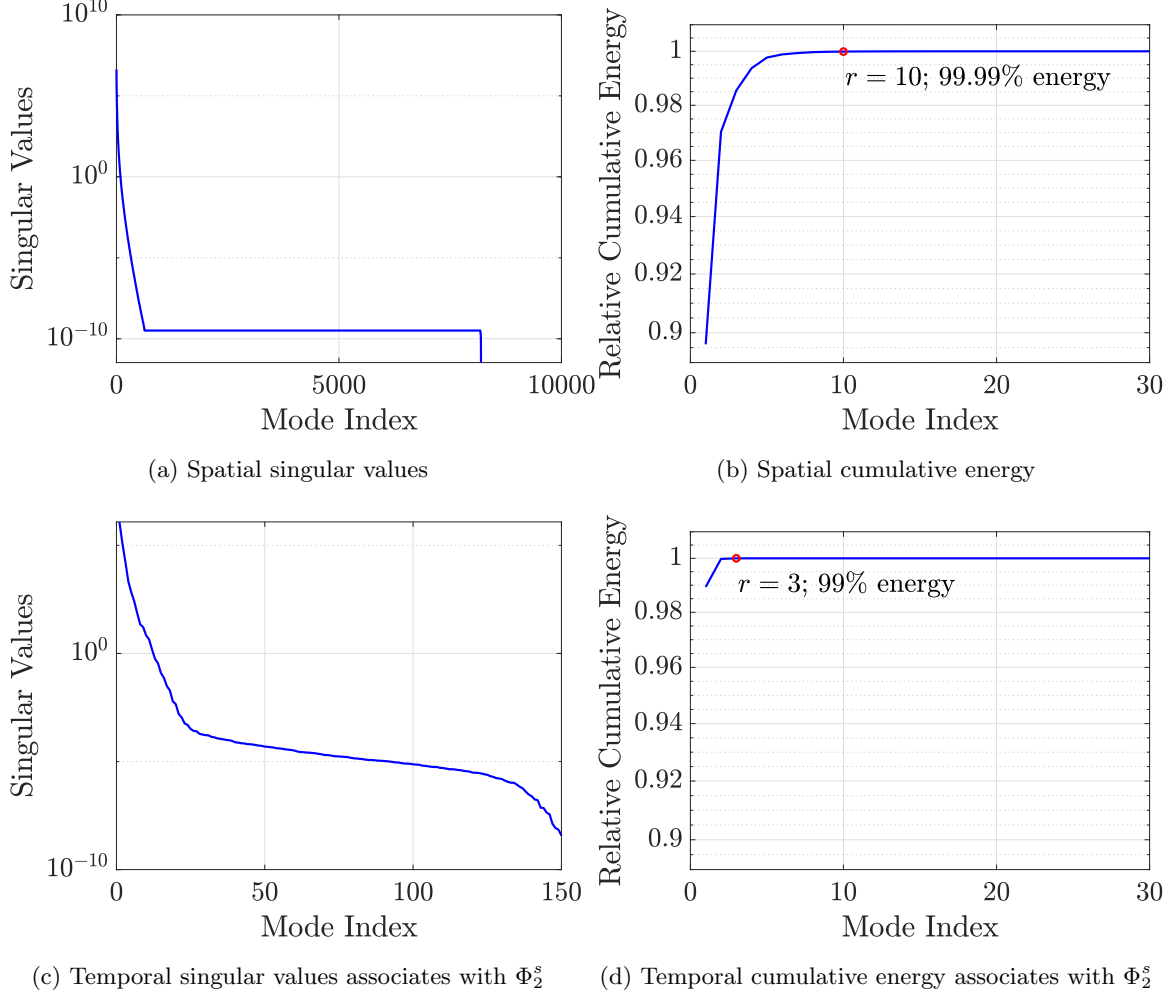


Figure 22: Reacting flow, singular values decomposition.

Table 11: Reacting flow, ST-ML-ROM methods performance at point $\mu_{\text{test}} = (5.9315 \times 10^{12}, 3.5416) \in \mathbf{D}_{\text{test}}$ for one online computation.

method	polynomial regression	kNN	random forest	neural network
configuration	2 nd order	3 neighbors	(max_leaf_nodes=116, n_estimators=81),	(n_hidden=10, n_neurons=19, learning_rate= 1.27×10^{-3} , activation=sigmoid)
# of ROM bases	60	60	60	60
rel. sol. error	3.4874×10^{-2}	8.1488×10^{-3}	4.8558×10^{-3}	7.7105×10^{-2}

10^{-3} , activation=sigmoid), respectively. Table 11 reports the chosen hyper-parameters and associated performance of the methods, while Figure 24 visualizes the ST-ML-ROM solutions and solution errors of the 2nd order polynomial regressor. The results on Table 11 and Figure 24 verify that our proposed methods

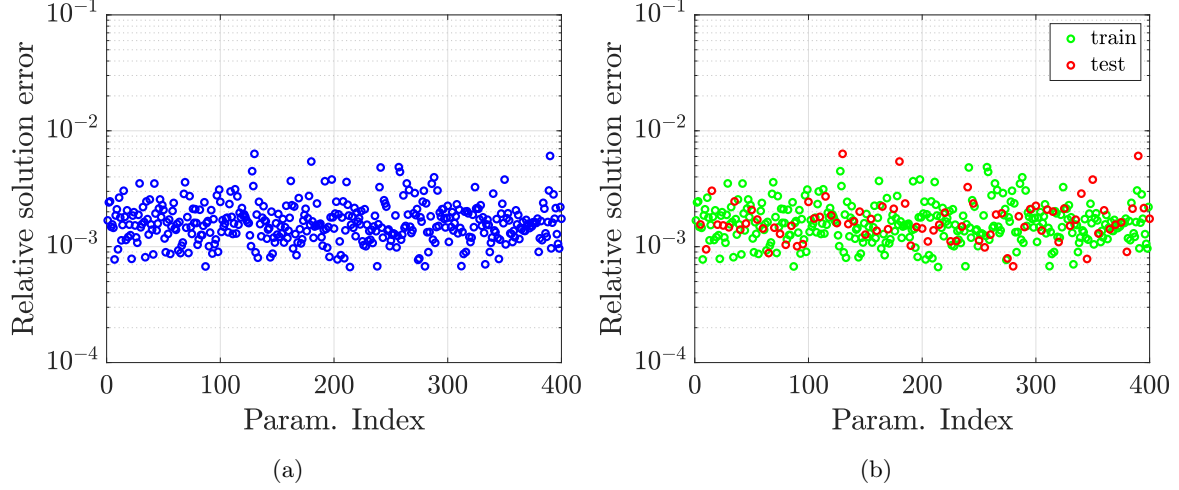


Figure 23: Reacting flow, “best” relative error for $\mu \in \mathcal{D}$ with $n_s = 20$, $n_t = 3$, $p = n_s n_t = 60$.

yield very accurate solutions.

5.3.4 ST-ML-ROM: parameter study

Table 12: Reacting flow, hyper-parameter ranges of cross-validation randomized search for random forest regressor

Hyper-parameters	Range/Limit
<code>max_leaf_nodes</code>	[10,1000]
<code>n_estimators</code>	[10,1000]

Table 13: Reacting flow, hyper-parameters of nine *best* configurations of random forest regressor

Hyper-parameters	config 1	config 2	config 3	config 4	config 5	config 6	config 7	config 8	config 9
<code>max_leaf_nodes</code>	709	109	967	885	815	116	624	710	286
<code>n_estimators</code>	985	881	696	576	395	81	131	30	170

Table 14: Reacting flow, hyper-parameter ranges of cross-validation randomized search for neural network regressor

Hyper-parameters	Range/Limit
<code>n_hidden</code>	{5,10,20,40,60}
<code>n_neurons</code>	[1,100]
<code>learning_rate</code>	$[10^{-4}, 10^{-1}]$
<code>activation</code>	{relu, tanh, sigmoid}

We again compare the performance of the ROM methods across a wide variation of all method parameters. In particular, the degree of polynomial regressor will be varied in the range $1 \leq r \leq 5$. For kNN regressor, the number of neighbors will be varied in the range $1 \leq k \leq 19$. For random forest and neural network regressors,

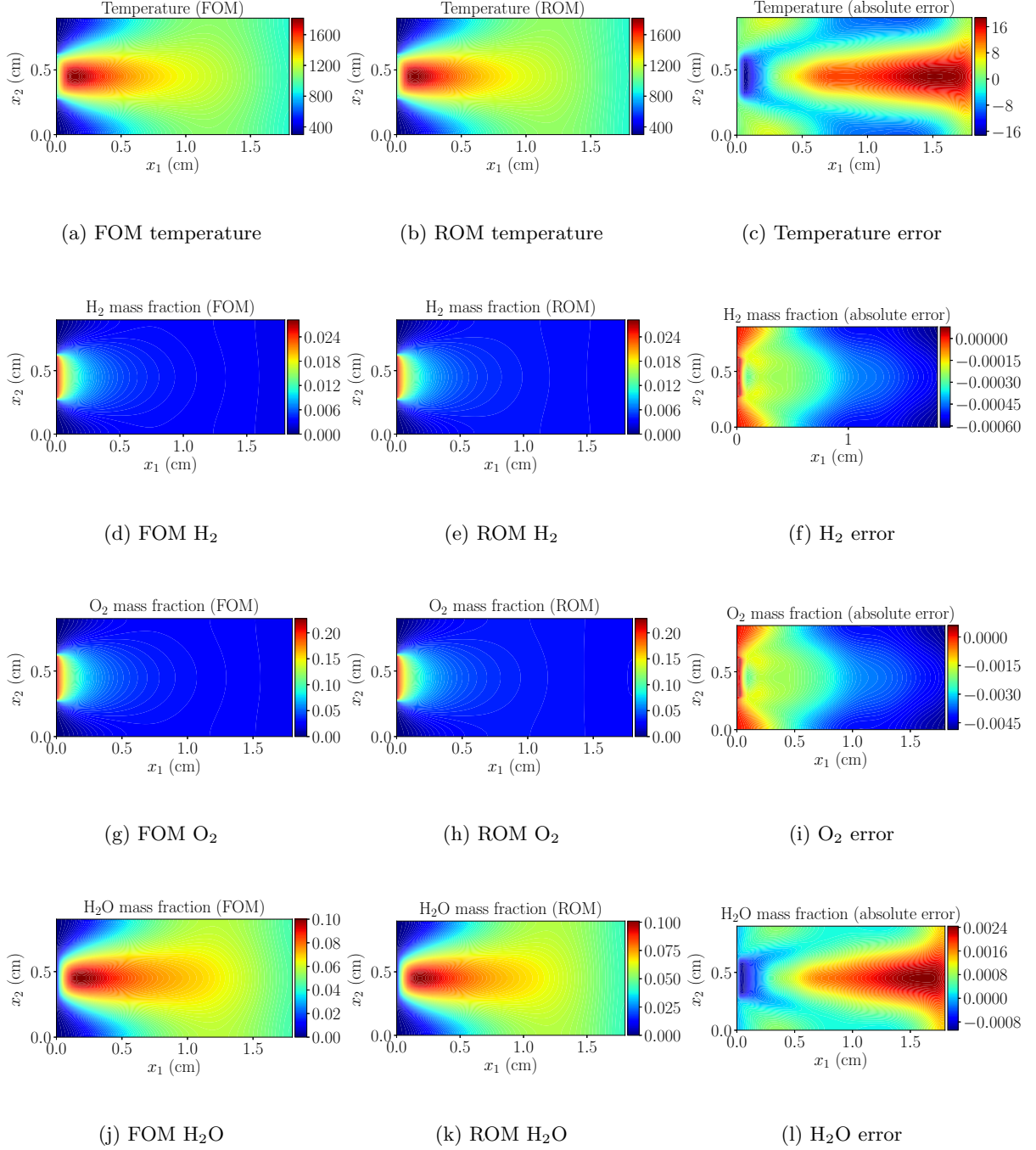


Figure 24: Reacting flow, solution visualization with 2nd order polynomial regressor at time $t = 0.039\text{sec}$, $\mu_{\text{test}} = (5.9315 \times 10^{12}, 3.5416) \in \mathbf{D}_{\text{test}}$ on Table 11.

we employ the same approach as described in Section 5.1.4 to find their *several* optimal configurations. In this spirit, the hyper-parameter limits of the cross-validation randomized searches for random forest and neural network regressors are listed on Table 12 and 14; while Table 13 and 15 report the hyper-parameter

Table 15: Reacting flow, hyper-parameters of nine *best* configurations of neural network regressor

Hyper-parameters	config 1	config 2	config 3	config 4	config 5	config 6	config 7
n_hidden	10	10	60	5	10	60	20
n_neurons	90	67	83	76	19	26	39
learning_rate	5.6173 $\times 10^{-2}$	1.6231 $\times 10^{-2}$	9.1173 $\times 10^{-3}$	3.1614 $\times 10^{-2}$	1.2702 $\times 10^{-3}$	1.4755 $\times 10^{-4}$	9.3875 $\times 10^{-2}$
activation	tanh	sigmoid	tanh	tanh	sigmoid	sigmoid	tanh

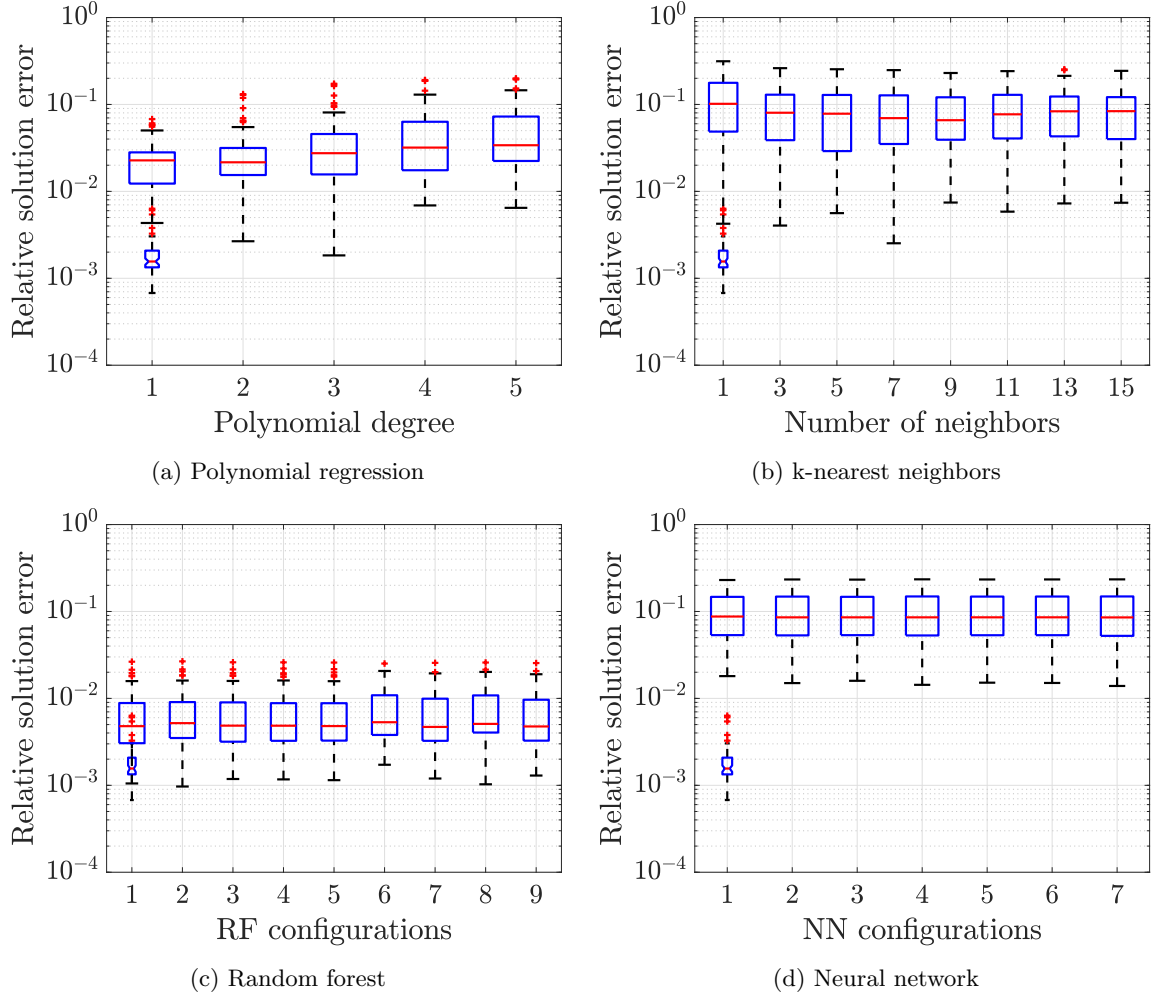


Figure 25: Reacting flow, relative solution error with $\mu \in \mathbf{D}_{\text{test}}$. The lowermost box is for “best” relative error defined in (4.1), and all upper boxes for ST-ML-ROM using four machine learning techniques.

values associated with their nine and seven *best* configurations after the randomized searches, respectively.

We then investigate the accuracy of these configurations by computing their relative solution errors together with the “best” relative error Eq. (4.1) for all $\mu \in \mathbf{D}_{\text{test}}$. Figure 25 reports all these relative solution errors. We observe from Figure 25 again that the proposed methods yield accurate solutions and reasonable error levels for engineering settings.

Finally, the computational time of the considered configurations are also investigated. We apply the same

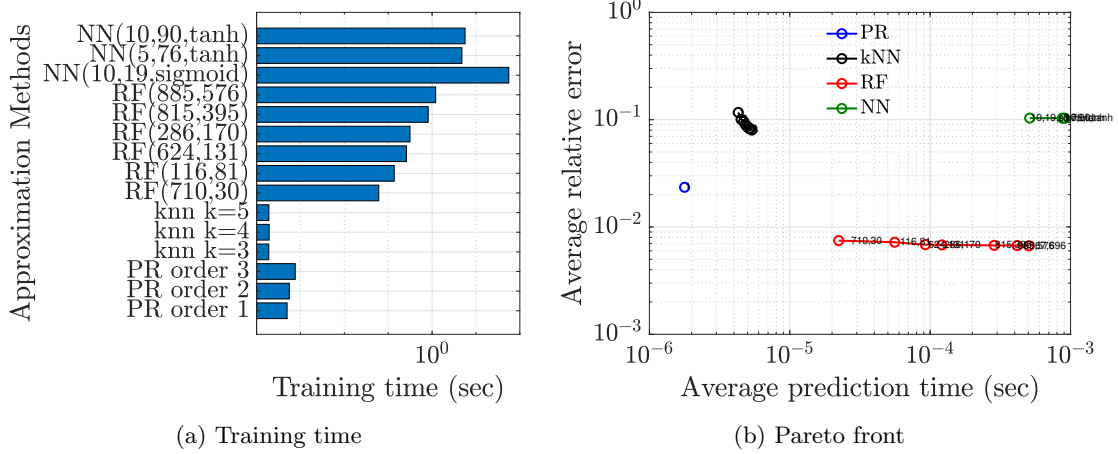


Figure 26: Reacting flow, training time and Pareto front of four ST-ML-ROM techniques: PR=Polynomial Regression, kNN=k-nearest neighbor, RF=Random Forest and NN=Neural Network.

procedure described in Section 5.1.4 to measure computational times; the same Table 7 lists the number of repeated offline and online runs for each configuration. Figure 26a and Figure 26b report the training time and Pareto front for online predictions, respectively. Again, Figure 26b shows a very similar trend to Figure 18b and 9c in which simple ML techniques (such as polynomial, kNN and random forest regressors) outperform complex ML ones (neural network) in terms of accuracy and computational cost; especially random forest is the best choice for this complicated problem.

6 Conclusion

Numerical experiments in this paper have demonstrated that the use of space-time subspace bases combined with machine learning methods provide a tractable and effective way to map between input parameters to a time-dependent high-dimensional output quantity of interest. The method can be applied straightforwardly to applications that exhibit a fast decaying Kolmogorov n -width⁶ (see other approaches, e.g., [63, 64, 65] to handle problems exhibiting slowly decaying Kolmogorov n -width). The numerical experiments in this paper have also highlighted the important point that the availability of data in an engineering setting is typically much less than it is in other machine learning applications. This is because engineering data are often generated from expensive physics-based codes or from sensors embedded on a physical system. In either case, it is reasonable to expect hundreds or thousands of training data points, but not millions as is the case in many non-engineering machine learning applications. The strategy to choose appropriate machine learning methods is thus affected by this fact. In particular, we have observed that in this setting simpler polynomial regression or random forest models may be better choices (than complicated neural networks) – even when the underlying physical phenomena exhibit strongly nonlinear behavior. Another possible reason explaining why polynomial regression, kNN and random forest provide more accurate solutions than neural network does (in this engineering setting) is that these 3 methods build one surrogate model for *each* mapping $\boldsymbol{\mu} \mapsto \alpha_i(\boldsymbol{\mu})$, $i \in \mathbb{N}(r)$ (hence totally r models to approximate whole mapping), while neural network build one unique surrogate model for the *whole* mapping $\boldsymbol{\mu} \mapsto \boldsymbol{\alpha}(\boldsymbol{\mu})$.

⁶The Kolmogorov n -width is defined as: $d_n(\mathcal{M}) := \inf_{S_n} \sup_{f \in \mathcal{M}} \inf_{g \in S_n} \|f - g\|$, where the first infimum is taken over all n -dimensional subspaces of the state space, and \mathcal{M} denotes the manifold of solutions over all time and parameters.

Acknowledgements

This paper describes objective technical results and analysis. Any subjective views or opinions that might be expressed in the paper do not necessarily represent the views of the U.S. Department of Energy or the United States Government. Sandia National Laboratories is a multimission laboratory managed and operated by National Technology and Engineering Solutions of Sandia, LLC., a wholly owned subsidiary of Honeywell International, Inc., for the U.S. Department of Energy's National Nuclear Security Administration under contract DE-NA-0003525.

References

- [1] Gallivan, K., Grimme, E., and Dooren, P. V., "Asymptotic waveform evaluation via a Lanczos method," Applied Mathematics Letters, Vol. 7, No. 5, 1994, pp. 75–80.
- [2] Silveira, L. M., Kamon, M., Elfadel, I., and White, J., "A coordinate-transformed Arnoldi algorithm for generating guaranteed stable reduced-order models of RLC circuits," Computer Methods in Applied Mechanics and Engineering, Vol. 169, No. 3-4, 1999, pp. 377–389.
- [3] Boley, D. L., "Krylov space methods on state-space control models," Circuits, Systems and Signal Processing, Vol. 13, No. 6, 1994, pp. 733–758.
- [4] Bai, Z., "Krylov subspace techniques for reduced-order modeling of large-scale dynamical systems," Applied numerical mathematics, Vol. 43, No. 1-2, 2002, pp. 9–44.
- [5] Willcox, K. and Peraire, J., "Balanced Model Reduction via the Proper Orthogonal Decomposition," AIAA JOURNAL, Vol. 40, No. 11, 2002.
- [6] Sirovich, L., "Turbulence and the dynamics of coherent structures. Part I: Coherent structures," Quarterly of applied mathematics, Vol. 45, No. 3, 1987, pp. 561–571.
- [7] Rozza, G., Huynh, D., and Patera, A. T., "Reduced basis approximation and a posteriori error estimation for affinely parametrized elliptic coercive partial differential equations," Archives of Computational Methods in Engineering, Vol. 15, No. 3, 2008, pp. 229–275.
- [8] Chinesta, F., Ladeveze, P., and Cueto, E., "A short review on model order reduction based on proper generalized decomposition," Archives of Computational Methods in Engineering, Vol. 18, No. 4, 2011, pp. 395.
- [9] Schmid, P. J., "Dynamic mode decomposition of numerical and experimental data," Journal of fluid mechanics, Vol. 656, 2010, pp. 5–28.
- [10] Astrid, P., Weiland, S., Willcox, K., and Backx, T., "Missing point estimation in models described by proper orthogonal decomposition," IEEE Transactions on Automatic Control, Vol. 53, No. 10, 2008, pp. 2237–2251.
- [11] Carlberg, K., Farhat, C., Cortial, J., and Amsallem, D., "The GNAT method for nonlinear model reduction: effective implementation and application to computational fluid dynamics and turbulent flows," Journal of Computational Physics, Vol. 242, 2013, pp. 623–647.
- [12] Barrault, M., Maday, Y., Nguyen, N. C., and Patera, A. T., "An 'empirical interpolation' method: application to efficient reduced-basis discretization of partial differential equations," Comptes Rendus Mathematique, Vol. 339, No. 9, 2004, pp. 667–672.
- [13] Chaturantabut, S. and Sorensen, D. C., "Nonlinear model reduction via discrete empirical interpolation," SIAM Journal on Scientific Computing, Vol. 32, No. 5, 2010, pp. 2737–2764.

- [14] Ly, H. V. and Tran, H. T., “Modeling and control of physical processes using proper orthogonal decomposition,” Mathematical and computer modelling, Vol. 33, No. 1-3, 2001, pp. 223–236.
- [15] Bui-Thanh, T., Damodaran, M., and Willcox, K., “Aerodynamic data reconstruction and inverse design using proper orthogonal decomposition,” AIAA journal, Vol. 42, No. 8, 2004, pp. 1505–1516.
- [16] Everson, R. and Sirovich, L., “Karhunen–Loève procedure for gappy data,” Journal of the Optical Society of America A, Vol. 12, No. 8, 1995, pp. 1657–1664.
- [17] Audouze, C., De Vuyst, F., and Nair, P., “Reduced-order modeling of parameterized PDEs using time-space-parameter principal component analysis,” International journal for numerical methods in engineering, Vol. 80, No. 8, 2009, pp. 1025–1057.
- [18] Audouze, C., De Vuyst, F., and Nair, P. B., “Nonintrusive reduced-order modeling of parametrized time-dependent partial differential equations,” Numerical Methods for Partial Differential Equations, Vol. 29, No. 5, 2013, pp. 1587–1628.
- [19] Wirtz, D., Karajan, N., and Haasdonk, B., “Surrogate modeling of multiscale models using kernel methods,” International Journal for Numerical Methods in Engineering, Vol. 101, No. 1, 2015, pp. 1–28.
- [20] Mainini, L. and Willcox, K., “Surrogate modeling approach to support real-time structural assessment and decision making,” AIAA Journal, Vol. 53, No. 6, 2015, pp. 1612–1626.
- [21] Ulu, E., Zhang, R., and Kara, L. B., “A data-driven investigation and estimation of optimal topologies under variable loading configurations,” Computer Methods in Biomechanics and Biomedical Engineering: Imaging & Visualization, Vol. 4, No. 2, 2016, pp. 61–72.
- [22] Hesthaven, J. S. and Ubbiali, S., “Non-intrusive reduced order modeling of nonlinear problems using neural networks,” Journal of Computational Physics, Vol. 363, 2018, pp. 55–78.
- [23] Chen, W., Hesthaven, J. S., Junqiang, B., Qiu, Y., Yang, Z., and Tihao, Y., “Greedy nonintrusive reduced order model for fluid dynamics,” AIAA Journal, Vol. 56, No. 12, 2018, pp. 4927–4943.
- [24] Swischuk, R., Mainini, L., Peherstorfer, B., and Willcox, K., “Projection-based model reduction: Formulations for physics-based machine learning,” Computers & Fluids, Vol. 179, 2019, pp. 704–717.
- [25] Ljung, L., “System identification,” Wiley encyclopedia of electrical and electronics engineering, 1999, pp. 1–19.
- [26] Viberg, M., “Subspace-based methods for the identification of linear time-invariant systems,” Automatica, Vol. 31, No. 12, 1995, pp. 1835–1851.
- [27] Reynders, E., “System identification methods for (operational) modal analysis: review and comparison,” Archives of Computational Methods in Engineering, Vol. 19, No. 1, 2012, pp. 51–124.
- [28] Mendel, J. M., “Tutorial on higher-order statistics (spectra) in signal processing and system theory: Theoretical results and some applications,” Proceedings of the IEEE, Vol. 79, No. 3, 1991, pp. 278–305.
- [29] Drmac, Z., Gugercin, S., and Beattie, C., “Vector fitting for matrix-valued rational approximation,” SIAM Journal on Scientific Computing, Vol. 37, No. 5, 2015, pp. A2346–A2379.
- [30] Proctor, J. L., Brunton, S. L., and Kutz, J. N., “Dynamic mode decomposition with control,” SIAM Journal on Applied Dynamical Systems, Vol. 15, No. 1, 2016, pp. 142–161.
- [31] Peherstorfer, B. and Willcox, K., “Data-driven operator inference for nonintrusive projection-based model reduction,” Computer Methods in Applied Mechanics and Engineering, Vol. 306, 2016, pp. 196–215.

- [32] Castelletti, A., Galelli, S., Restelli, M., and Soncini-Sessa, R., “Data-driven dynamic emulation modelling for the optimal management of environmental systems,” Environmental Modelling & Software, Vol. 34, 2012, pp. 30–43.
- [33] Balzano, L., Nowak, R., and Recht, B., “Online identification and tracking of subspaces from highly incomplete information,” 2010 48th Annual allerton conference on communication, control, and computing (Allerton), IEEE, 2010, pp. 704–711.
- [34] Peherstorfer, B. and Willcox, K., “Online adaptive model reduction for nonlinear systems via low-rank updates,” SIAM Journal on Scientific Computing, Vol. 37, No. 4, 2015, pp. A2123–A2150.
- [35] Brunton, S. L., Proctor, J. L., and Kutz, J. N., “Discovering governing equations from data by sparse identification of nonlinear dynamical systems,” Proceedings of the national academy of sciences, Vol. 113, No. 15, 2016, pp. 3932–3937.
- [36] Dean, S., Mania, H., Matni, N., Recht, B., and Tu, S., “On the sample complexity of the linear quadratic regulator,” Foundations of Computational Mathematics, 2019, pp. 1–47.
- [37] Wang, Q., Hesthaven, J. S., and Ray, D., “Non-intrusive reduced order modeling of unsteady flows using artificial neural networks with application to a combustion problem,” Journal of computational physics, Vol. 384, 2019, pp. 289–307.
- [38] Fresca, S., Dede, L., and Manzoni, A., “A comprehensive deep learning-based approach to reduced order modeling of nonlinear time-dependent parametrized PDEs,” arXiv preprint arXiv:2001.04001, 2020.
- [39] Renganathan, S. A., Maulik, R., and Rao, V., “Machine learning for nonintrusive model order reduction of the parametric inviscid transonic flow past an airfoil,” Physics of Fluids, Vol. 32, No. 4, 2020, pp. 047110.
- [40] Kast, M., Guo, M., and Hesthaven, J. S., “A non-intrusive multifidelity method for the reduced order modeling of nonlinear problems,” Computer Methods in Applied Mechanics and Engineering, Vol. 364, 2020, pp. 112947.
- [41] Rajaram, D., Puranik, T. G., Perron, C., and Mavris, D. N., “Non-Intrusive Parametric Reduced Order Modeling using Randomized Algorithms,” AIAA Scitech 2020 Forum, 2020, p. 0417.
- [42] Fritzen, F. and Hassani, M., “Space–time model order reduction for nonlinear viscoelastic systems subjected to long-term loading,” Meccanica, Vol. 53, No. 6, 2018, pp. 1333–1355.
- [43] Choi, Y. and Carlberg, K., “Space–Time Least-Squares Petrov–Galerkin Projection for Nonlinear Model Reduction,” SIAM Journal on Scientific Computing, Vol. 41, No. 1, 2019, pp. A26–A58.
- [44] Carlberg, K., Bou-Mosleh, C., and Farhat, C., “Efficient non-linear model reduction via a least-squares Petrov–Galerkin projection and compressive tensor approximations,” International Journal for Numerical Methods in Engineering, Vol. 86, No. 2, 2011, pp. 155–181.
- [45] Carlberg, K., Barone, M., and Antil, H., “Galerkin v. least-squares Petrov–Galerkin projection in nonlinear model reduction,” Journal of Computational Physics, Vol. 330, 2017, pp. 693–734.
- [46] Hoang, C., Choi, Y., and Carlberg, K., “Domain-decomposition least-squares Petrov-Galerkin (DD-LSPG) nonlinear model reduction,” arXiv preprint arXiv:2007.11835, 2020.
- [47] Vannieuwenhoven, N., Vandebril, R., and Meerbergen, K., “A new truncation strategy for the higher-order singular value decomposition,” SIAM Journal on Scientific Computing, Vol. 34, No. 2, 2012, pp. A1027–A1052.

- [48] Austin, W., Ballard, G., and Kolda, T. G., “Parallel tensor compression for large-scale scientific data,” 2016 IEEE international parallel and distributed processing symposium (IPDPS), IEEE, 2016, pp. 912–922.
- [49] Carlberg, K., Ray, J., and van Bloemen Waanders, B., “Decreasing the temporal complexity for non-linear, implicit reduced-order models by forecasting,” Computer Methods in Applied Mechanics and Engineering, Vol. 289, 2015, pp. 79–103.
- [50] Carlberg, K., Brencher, L., Haasdonk, B., and Barth, A., “Data-driven time parallelism via forecasting,” SIAM Journal on Scientific Computing, Vol. 41, No. 3, 2019, pp. B466–B496.
- [51] Bentley, J. L., “Multidimensional binary search trees used for associative searching,” Communications of the ACM, Vol. 18, No. 9, 1975, pp. 509–517.
- [52] Friedman, J. H., Bentley, J. L., and Finkel, R. A., “An algorithm for finding best matches in logarithmic expected time,” ACM Transactions on Mathematical Software (TOMS), Vol. 3, No. 3, 1977, pp. 209–226.
- [53] Géron, A., Hands-on machine learning with Scikit-Learn, Keras, and TensorFlow: Concepts, tools, and techniques to build intelligent systems, O’Reilly Media, 2019.
- [54] Breiman, L., Friedman, J., Stone, C. J., and Olshen, R. A., Classification and regression trees, CRC press, 1984.
- [55] Nielsen, M. A., Neural networks and deep learning, Vol. 2018, Determination press San Francisco, CA, 2015.
- [56] Rumelhart, D. E., Hinton, G. E., and Williams, R. J., “Learning representations by back-propagating errors,” nature, Vol. 323, No. 6088, 1986, pp. 533–536.
- [57] Livni, R., Shalev-Shwartz, S., and Shamir, O., “On the computational efficiency of training neural networks,” Advances in neural information processing systems, 2014, pp. 855–863.
- [58] Pedregosa, F., Varoquaux, G., Gramfort, A., Michel, V., Thirion, B., Grisel, O., Blondel, M., Prettenhofer, P., Weiss, R., Dubourg, V., Vanderplas, J., Passos, A., Cournapeau, D., Brucher, M., Perrot, M., and Duchesnay, E., “Scikit-learn: Machine Learning in Python,” Journal of Machine Learning Research, Vol. 12, 2011, pp. 2825–2830.
- [59] Grepl, M. A., Maday, Y., Nguyen, N. C., and Patera, A. T., “Efficient reduced-basis treatment of nonaffine and nonlinear partial differential equations,” ESAIM: Mathematical Modelling and Numerical Analysis, Vol. 41, No. 03, 2007, pp. 575–605.
- [60] Budiman, M., “Latin Hypercube Sampling, MATLAB Central File Exchange,” <https://www.mathworks.com/matlabcentral/fileexchange/4352-latin-hypercube-sampling>, July 2020.
- [61] scikit-learn 0.24.0, “Randomized Search Cross Validation,” https://scikit-learn.org/stable/modules/generated/sklearn.model_selection.RandomizedSearchCV.html, Dec. 2020.
- [62] MatlabR2020b, “Malab cvpartition command,” <https://www.mathworks.com/help/stats/cvpartition.html>, Dec. 2020.
- [63] Lee, K. and Carlberg, K., “Deep Conservation: A latent dynamics model for exact satisfaction of physical conservation laws,” arXiv preprint arXiv:1909.09754, 2019.
- [64] Lee, K. and Carlberg, K. T., “Model reduction of dynamical systems on nonlinear manifolds using deep convolutional autoencoders,” Journal of Computational Physics, Vol. 404, 2020, pp. 108973.
- [65] Kim, Y., Choi, Y., Widemann, D., and Zohdi, T., “A fast and accurate physics-informed neural network reduced order model with shallow masked autoencoder,” arXiv preprint arXiv:2009.11990, 2020.